Development of fast-dissociating recombinant antibodies for high-density multiplexed IRIS super-resolution microscopy

Qianli Zhang

Contents

Abbreviations

Ala or A	Alanine
Calrt	Calreticulin
CBB	*Coomassie* Brilliant Blue
CDR	Complementarity Determining Region
CMV	Cytomegalovirus
EGFP	Enhanced Green Fluorescent Protein
FR	Frame-work Region of antibody
Gly or G	Glycine
H2Bb	Histone 2B
hNido	human Nidogen1
IRIS	Image Reconstruction by Integrating exchangeable Single-molecule localization
k_{off}	Dissociation rate
K_{pb}	Photobleaching rate of EGFP
mIgH	mouse IgH
mNido	mouse Nidogen1
MRLC	Myosin Regulatory Light Chain 2
PAINT	Point Accumulation In Nanoscale Topography
PALM	Photoactivated Localization Microscopy
PDB	Protein Data Bank
POC	Phase-Only Correlation
scFv	Single-chain variable fragment
SIM	Structured Illumination Microscopy
SMLM	Single-Molecule Localization super-resolution Microscopy
STED	Stimulated Emission Depletion Microscopy
STORM	Stochastic Optical Reconstruction Microscopy
$T_{1/2}$	Dissociation half-life
Tyr or Y	Tyrosine
V_H	Variable Heavy chain
V_L	Variable Light chain

Abstract

I developed a versatile mutagenesis strategy that can effectively increase the dissociation rate of antibodies by orders of magnitude without compromising the binding specificity. Single-molecule localization super-resolution microscopy (SMLM) has greatly surpassed the diffraction limit of conventional optical microscopy. The imaging fidelity and labelling density, however, are limited by spatial interference between bulky antibodies in a confined resolved area. Image reconstruction by integrating exchangeable single-molecule localization (IRIS) has overcome the problem using exchangeable probes that transiently bind to endogenous targets. In our previous research, generation of fast-dissociating IRIS probes has been challenging. In this study, I report a new mutagenesis strategy that make it feasible to generate IRIS probes from the repository of off-the-shelf antibodies. I successfully generated dozens of IRIS probes and demonstrate multiplexed localization of endogenous proteins in primary neurons that visualizes small synaptic connections. The fast-dissociating probes based IRIS imaging achieved 4-fold higher label density than conventional super-resolution approaches and thus could visualize the feature of synaptic components with higher fidelity.

Chapter 1 Introduction

Section 1.1 Single-Molecule localization microscopy

The proverb says that "Seeing is believing". This proverb is suitable for scientific research. Fluorescent microscopy is a powerful tool to investigate small objects and structures in biological research because of its advantage of non-invasive and time-resolved imaging with high biochemical specificity[1]. However, due to the diffraction limit of light, the resolution in conventional light microscopy is limited to a lateral resolution of $d = \lambda / 2NA$ (~200 nm), where λ is the wavelength of light and NA is the numerical aperture of a lens[2]. In the recent 20 years, super-resolution fluorescence microscopy approaches have been developed to overcome the diffraction limit, including stimulated emission depletion microscopy (STED)[3], structured illumination microscopy (SIM)[4] and single-molecule localization microscopy (SMLM)[5].

SMLM improves the resolution to ~20-50 nm by localizing centroid of fluorophores and reconstructing the localizations. SMLM has many variations, such as fluorescence photoactivated localization microscopy (PALM), stochastic optical reconstruction microscopy (STORM) and point accumulation in nanoscale topography (PAINT). The resolution of SMLM is determined by the distance between adjacent fluorescent probes in a sample. According to the Nyquist criterion, structural features smaller than twice that of the labelled target distance cannot be reliably discerned[6]. Labeling density thus could become a limiting factor of the resolution[6,7]. Recently, our lab developed a novel localization super-resolution microscopy, IRIS, which achieved multiplexed high-fidelity imaging of cytoskeleton using fast-dissociating exchangeable probes[6]. IRIS probes could transiently associate with and dissociate from their targets directly in a biological sample. Theoretically, every endogenous target has the chance to be labelled with enough long period of imaging. In addition, IRIS probes can be easily removed by gentle washing, which allows multiplex imaging without cumulative damage to the sample. The initial IRIS probes were derived from peptide ligands of endogenous target proteins and could not be used to observe targets without known ligands. In order to expand the observation targets, I started to develop a more universal probe form that is antibody-based IRIS probe.

Section 1.2 Development of antibody-based IRIS probe

A concept that rapidly dissociable antibody can be used as exchangeable probes in IRIS microscopy has been raised in our laboratory. Similar to the protein ligands, antibodies can specifically associate with and dissociate from the target proteins (antigens). However, fast-dissociating antibodies that could transiently bind to antigens were hardly reported because these

antibodies tend to have a low affinity and are easy to be overlooked by conventional affinity-based assay, usually ELISA[8].

In the February of 2021, we reported a systematic kinetic-based screening assay to isolate fast-dissociating yet specific monoclonal antibodies against various antigens from hybridoma cell lines (co-first authorship)[8]. I successfully obtained dozens of fast-dissociating antibodies using the pipeline and showed that fluorescent labelled Fab fragments of these antibodies (Fab probes) could recognize over-expressed epitopes in cultured cells. I also performed 8-color super-resolution imaging of cells and 3-color imaging of inner ear tissues using these Fab probes (Fig. 1).

During the development of the Fab probes, I realized that the culture of hybridoma cells and the validation processes were still time-consuming and challenging. Expressing and purifying recombinant antibodies in commonly used cell lines, such as HEK293T cells, would largely simplify the validation and production process. Furthermore, generating recombinant probes from existing antibody sequences could greatly expand the usability of IRIS, but such an approach would require an efficient strategy to optimize the dissociation of the antibody-target interactions without compromising the binding specificity.

Section 1.3 Antibody fragment and recombinant antibody

Fv and nanobody are small antibody fragments that only contain the antigen binding domains. They are widely applied for a variety of biological assays and therapeutic applications owing to the specific binding properties of these nanoscopic molecules. When used in SMLM, these small antibody fragments could improve the accuracy of localization by reducing the distance between the fluorophores and the target proteins[9].

The Fv fragment of antibody is responsible for binding to the antigen, containing only two variable chains: V_H and V_L. The binding specificity of antibody is mainly regulated by the six complementarity determining regions (CDRs) that form loops on the variable heavy chain (V_H) and light chain (V_L). While, the framework region (FR) supports the binding of the CDR to the antigen[10] and maintains the overall structure of the variable domains on the antibody[11]. A major challenge in antibody optimization is the trade-off between antibody affinity, specificity, stability and solubility. For instance, enhanced affinity sometimes leads to deteriorated specificity and stability.

Individual Fv fragments are unstable due to the insufficient interaction between V_H and V_L domains. As a work-around, a single-chain variable fragment (scFv) is a commonly used recombinant Fv, in which the VH and VL of the antibody are connected with a short linker peptide. However, scFv cannot be adapted to all antibodies without stability engineering[12]. Moreover, scFvs have a reduced stability under thermal stress, which may limit their potential as an imaging tool[13]. In order to enhance

the structural stability of the Fv fragment, a universally applicable antibody fragment format, Fv-clasp, was constructed by fusing a coiled-coil SARAH domain of human Mst1 kinase to each chain of the variable region[14]. Fv-clasp constructs exhibit excellent compatibility and stability while retaining the binding affinity of the original antibodies, and can be used for immunostaining[15].

Section 1.4 New insight in this research

In this thesis, we introduce an efficient strategy to generate IRIS probes by site-specific mutagenesis of the common residues within V_H and V_L domains in the format of Fv-clasp or nanobody. Eight IRIS probes coupled with a set of peptide tags and two neuronal proteins were generated by modifying antibody cDNAs from hybridoma clones and open-source antibody sequences. These mutated antibody fragments retained their specificity and were usable for IRIS super-resolution microscopy by conjugating fluorescent proteins to their C-terminus. The method enables rapid conversion of existing antibody sequences to fast-dissociating probes for multiplexed high-density super-resolution imaging and will greatly expand the repository of IRIS probes.

Chapter 2 Materials and Methods

Section 2.1 Cell culture

Xenopus laevis XTC cells were maintained in Leibovitz's L15 medium (Thermo Fisher Scientific) diluted to 70% with sterilized water and supplemented with 10% fetal bovine serum (FBS, Gibco) as previously described[16]. HEK293T cells were cultured in Dulbecco's modified eagle medium (DMEM, Nacalai tesque) containing 10% FBS. Expi293F suspension cells (Thermo Fisher Scientific) were cultured in Expi293 expression medium (Thermo Fisher Scientific) according to the manufacturer's instruction.

Section 2.2 Transfection

Transfection of expression vectors containing epitope-tagged actin into XTC cells in 6-well dish by Neon Transfection System (Invitrogen) were performed according to the manufacture's instruction. Transfection of mammalian expression vectors containing Fv-clasps into HEK293T cells in 10 cm petri dish by using Lipofectamine 3000 (Thermo Fisher Scientific).

Section 2.3 Primary culture of neurons

Embryonic day 20 (E20) Wistar rats were purchased from Japan SLC, Inc., and were anesthetized by ISOFLURANE Inhalation Solution (Pfizer). Cerebrum and hippocampus were then isolated from brain and digested with trypsin. Cell suspension of hippocampus for neuron culture was incubated on Polyetherimide (PEI) coated glass slip. Cell suspension of cerebrum used for microglia culture was then filtered by 100 μm cell-strainer and pipetted to kill neurons. Filtered cell was incubated on Poly-L-Lysine (PLL) coated glass slip. MEM medium (Gibco) with 200nM L-Glutamine, 100nM Na-pyruvate and 2% NeuroBrew (Milteny) was used for neuron culturing and Neurobasal medium (Gibco) with 200nM L-Glutamine (Gibco), 100nM Na-pyruvate and 2% NeuroBrew was used for maintenance of neuron after DIV2. High Glucose DMEM medium (Nacalai) with 10% FBS and 1% penicillin-Streptomycin was used for microglia culture. All experiments were performed in accordance with the National Institutes of Health Guidelines for the Care and Use of Laboratory Animals and were approved by the Animal Research Committee of Kyoto University Graduate School of Medicine (No. 17555, Kyoto, Japan).

Section 2.4 cDNA

cDNAs of human vinculin (GenBank: BC039174)[17], Xenopus laevis paxillin (GenBank: BC070716), Xenopus laevis alpha-actinin (GenBank: BC043995) and human zyxin (GenBank: BC010031) were obtained from Open Biosystems. A cDNA encoding Xenopus laevis myosin light chain (NM_001086846.1) was artificially synthesized. cDNAs encoding Homer1, VGLUT1 and PSD95 were cloned from a mouse brain cDNA library (Takara-bio).

An EGFP cDNA was added to the heavy chain of Fv-clasp between SARAH domain and 6xHis tag by AgeI. Antibody sequences of 11G9, V302A and S66B were cloned from hybridoma cell lines[8], using primer sets as below[18]. The antibody cDNA of 2H8[19], NbALFA[20], HS69[21] and NV-Nb9[22] were artificially synthesized. Antibody sequence of L8/15 was a gift from James Trimmer (Addgene plasmid # 140071).

Primer for V_H cloning (5' - 3')	Primer for V_L cloning (5' - 3')
GATGTGAAGCTTCAGGAGTC	GATGTTTTGATGACCCAAACT
CAGGTGCAGCTGAAGSAGTC	GATATTGTGATRACSCAG
CAGGTTACTCTGAAAGAGTC	GACATTGTGMTGACCCARTCT
GAGGTCCAGCTGCARCAGTC	GATATTGTGCTAACTCAGTCT
CAGGTCCAACTGCAGCAGCCT	GAYATCCAGMTGACWCAGWCT
GAGGTGAAGCTGGTGGARTC	CAAATTGTTCTCACCCAGTCT
GATGTGAACTTGGAAGTGTC	CCGTTTCAGCTCCAGCTTG
TGCAGAGACAGTGACCAGAGT	CCGTTTTATTTCCARCTTTG
TGAGGAGACKGTGASHGWGGT	GGATACAGTTGGTGCAGCATC

Section 2.5 Expression plasmid construction

The expression vectors for XTC cells, pEGFP-C1, pEGFP-actin, were purchased from Clontech. These vectors were used to express epitope-tagged proteins after replacing the EGFP sequences with epitope tags. Cytomegalovirus (CMV) promoter of pFLAG-actin was truncated (delCMV) to lower cytotoxicity[16]. Expression vectors for P20.1 and 12CA5 Fv-clasp (v2) were obtained from a previous study[14]. The original signal peptide was replaced with a mouse IgH signal sequence as previously reported[23].

Section 2.6 Production and purification of AAV

The adeno-associated virus (AAV) vectors pAAV-hSyn1-mCherry or pAAV-hSyn1-mCherry-PSD95 were co-transfected with pAdDeltaF6 (helper) and AAV-PHP.eB Cap, which provide AAV with replication protein and capsid protein, respectively, into HEK293FT cells (Invitrogen) using 293fectin transfection reagent (Invitrogen). The supernatant was collected after 72 hours, centrifuged

at 1500 g for 30 minutes and then filtered through a 0.45μm syringe filter (Sartorius) as described previously (Chen et al., 2018). AAV in the supernatant was precipitated by adding AAVanced Concentration Reagent (SBI) for 24-72 hours. After precipitation, the suspension was centrifuged at 1,500 g for 30 minutes, and the supernatant was removed by aspiration. The pellet was resuspended in phosphate-buffered saline (PBS) and then vortexed.

Section 2.7 Antibody sequence alignment

Antibody and nanobody sequences for frequency analysis were obtained from PDB. CDRs of antibodies were defined using the Chothia Numbering Scheme[24]. Nanobody sequences were aligned using the ANARCI web server[25] in the Chothia numbering scheme. Nanobody CDRs were defined according to the previously described rules based on Chothia numbering[26].

Section 2.8 Recombinant antibody purification

For the purification of EGFP-conjugated Fv fragments, VH-SARAH-EGFP and VL-SARAH were co-transfected into HEK293T cells at a 1 : 1 molar ratio using a Lipofectamine 3000 Transfection Kit (ThermoFisher Scientific). EGFP conjugated nanobodies were transfected into HEK293 cells using the same kit. Culture supernatants were collected 4-5 days after the transfection. Antibody fragments in the supernatants were collected with Ni-NTA agarose (QIAGEN) at room temperature for 2 hours, washed three times with ice-cold Tris Buffered Saline (TBS; 20 mM Tris, 150 mM NaCl, pH 7.5) and once with TBS containing 10 mM imidazole (Nacalai Tesque, Inc). Bound antibody fragments were eluted with 200 mM imidazole in TBS. The purified polypeptides were dialyzed vs. TBS using Spectra/por membrane (MWCO: 6-8 kD, Spectrum Laboratories, Inc.), with two exchanges of buffer overnight at 4 ℃.

Section 2.9 Preparation of imaging sample

XTC cells expressing epitope-tagged actin and focal adhesion proteins were spread on coverslips coated with 100 μg/ml poly-L-lysine (Sigma) and 10 μg/ml fibronectin (Sigma) for 1 h to ensure the formation of flat lamellipodia and lamella. Next, the cells were fixed with 3. 7% PFA in cytoskeleton buffer (10 mM MES, 90 mM KCl, 3 mM $MgCl_2$, 2 mM EGTA, pH 6.1) containing 0.5% Triton-X100 (Nacalai tesque) for 20 min, then blocked with 3% BSA (Nacalai tesque) in PBS. XTC cells expressing Homer1 and VGLUT1 and primary cultured neuron were fixed with 4% PFA in PBS (Nacalai Tesque) containing 4% sucrose for 30 min, permeabilized with PBS containing 0.15% Triton-X100 for 10 min and blocked with 3% BSA in PBS[27]. For the imaging of axonal actin rings,

neurons were initially fixed for 1 min using a solution of 0.3% glutaraldehyde and 0.25% Triton X-100 in cytoskeleton buffer (CB, 10 mM MES, pH 6.1, 150 mM NaCl, 5 mM EGTA, 5 mM glucose and 5 mM $MgCl_2$), and then post-fixed for 15 min in 2% glutaraldehyde in CB, which is a previously described method[28].

Section 2.10 Buffer for single-molecule imaging

For measuring dissociation rate, probes were applied at 0.05 – 0.1 nM in HEPES-KCl-Tx buffer (10 mM HEPES-KOH, 90 mM KCl, 3 mM $MgCl_2$, 0.1 mM dithiothreitol, 0.2% Triton-X100, pH 7.2) with an oxygen scavenging mixture (0.2 mg/mL glucose oxidase, 0.035 mg/mL catalase, 0.45% glucose, 0.5% 2-mercaptoethanol)[8].

For IRIS imaging, probes were applied in 50mM Tris buffer (pH 8.0)[29], with an oxygen scavenging mixture containing 5 U/ml pyranose oxidase (Sigma-Aldrich)[30], 10 mM mercaptoethylamine (Sigma-Aldrich)[31], 60 ug/ml catalase (Sigma-Aldrich) and 10% glucose[31].

Section 2.11 Microscopy

Time-lapse imaging of single-molecules bound to fixed XTC cells expressing epitope tagged actin or target proteins were acquired under 488-nm illumination with an Olympus IX83 inverted microscope equipped with an IX3-ZDC2 Z-drift compensator (Olympus), a UPlansApo 100, 1.40 NA oil objective (Olympus), an Evolve 512 EMCCD camera (Roper Scientific) and an Cobolt Blues 50 mW laser (488 nm; Cobolt).

Single-molecule stream acquisition for primary neuron was acquired under 488-nm illumination with an Olympus IX83 inverted microscope equipped with an IX3-ZDC2 Z-drift compensator (Olympus), an UPlanApo 60x/1.50 NA oil HR objective (Olympus), ORCA-Flash4.0 V3 Digital CMOS camera (Hamamatsu). The laser system is equipped with an OBIS 488 nm 150 mW Laser (Coherent), an OBIS 552 nm 150 mW Laser (Coherent) and a gem 671 nm 750 mW Laser (Laser Quantum).

Section 2.12 Determination of dissociation rate

Bound antibody fragments in the first frame of the time-lapse stack were tracked by a python program (https://github.com/takushim/tanitracer) as previously reported[8]. Dissociation rates of antibody fragments were determined by fitting the regression of bound antibody fragments to one-phase decay models ($y = Y0 \times \exp(-k_{off} \times t)$) using Prism 7.0. The dissociation rate was corrected by

subtracting the photobleaching rate K from the measured k_{off} values. The half-life ($T_{1/2}$) is the time needed to let dissociate half of the probes from the targets. It is calculated as $T_{1/2} = \ln 2 / k_{off}$.

Section 2.13 Super-resolution analysis

Spots in the single-molecule images were tracked and plotted on the blank image arrays using python programs (https://github.com/takushim/tanitracer) as previously reported[8]. For determination of binding events in Homer and VGLUT puncta, each binding probe was consolidated to the average position. Spots which last shorter than three frames were filtered to reduce the noise and improve the localization precision. The possibility of being labelled (p) was calculated using binomial distribution $p = 1 - ((m - 1) / m)^n$, where m is the molecule number of target protein and n is the label number. One "label" refers to a binding (on-off) event of IRIS probe to target protein. Resolution of images were evaluated using free decorrelation analysis plugin in ImageJ[32]. Stage drift was compensated using phase-only correlation (POC) with discrete Fourier transform for cell samples[33].

Chapter 3 Results

Section 3.1 Optimizing the secretion efficiency of Fv-clasp

I obtained a set of epitope tag-specific antibody sequences from previous studies, including P20.1 (anti-TARGET tag)[34], 12CA5 (anti-HA tag)[14], 2H8 (anti-FLAG tag)[19], V302A (anti-V5 tag)[8], S66B (anti-S tag)[8] and 11G9 (anti-FLAG tag)[8]. These antibody sequences were incorporated into Fv-clasp vectors as shown in Fig. 2A.

To optimize the productivity of Fv-clasp in secretion form, I compared the yield of P20.1 Fv-clasp which were expressed using signal peptides from mouse Nidogen1 (mNido)[35], human Nidogen1 (hNido)[36], mouse IgH (mIgH)[37,38] and Calreticulin (Calrt)[39], respectively (Fig. 2B). Only a little Fv-clasp was secreted using hNido. The amount of Fv-clasp in culture supernatant of mIgH was approximately three times more than mNido and Calrt. Therefore, I adopted the signal peptide of mIgH for the following experiment of recombinant antibody production.

Section 3.2 Construction and purification of recombinant Fv-EGFP

I constructed 'Fv-EGFP' by fusing EGFP to the C-terminus of the heavy chain of Fv-clasp and purified the expressed fusion protein from the culture supernatant of HEK293T cells (Fig. 2C). The expression of EGFP conjugated Fv-clasp could be observed in the cells (Fig. 2D). The Fv-EGFP in the supernatant was purified using 6x His tag and was then subjected to CBB (*Coomassie* Brilliant Blue) staining (Fig. 2E). The size of purified Fv-EGFP dimmer (Fig. 2E, band c), heavy chain (band a) and light chain (band b) were consistent with their molecular weights (heavy chain: ~47.5 kDa; light chain: ~19.5 kDa). There is almost no degradation or aggregation in the product even I did not use chromatography for purification. The purified Fv-EGFPs were used as fluorescent probes in the following single-molecule imaging assays. HEK293T cells in a 10 cm petri dish typically yield 0.34 - 4.02 μg (5 - 60 pmol) Fv-EGFP, which were enough for 20 - 60 times imaging. The purified probes were mostly fluorescent because the concentration measured by fluorescent intensity was comparable to the concentration determined by CBB protein assay.

Section 3.3 Determination of the dissociation rate by single-molecule imaging

All Fv-EGFPs recognized the relevant expressed epitope-tagged actin in *Xenopus laevis* XTC cells after fixation (Fig. 3A). I determined the dissociation rate (k_{off}) by tracking the single-molecule Fv-EGFPs that bound to epitope-tagged actin and fitting the regression curve to one phase decay model. I also measured the photobleaching rate of EGFP (K_{pb}) in fixed XTC (Fig. 3B). The k_{off} was

corrected by subtracting the K_{pb} from the measured dissociation rate and the results were listed up in Fig. 3C. The k_{off} values are consistent with previous studies[8,14,40].

Section 3.4 Accelerating the dissociation rate of Fv-EGFP and Nanobody

To achieve high fidelity IRIS imaging of intracellular proteins, probes that dissociate in a few seconds are desirable. I therefore sought to increase the dissociation rate of P20.1, 12CA5, 2H8, V302A and S66B by site-directed mutagenesis. I premised the strategy on the notion that candidate sites for mutagenesis should be commonly conserved in antibodies and would minimally impact specificity.

With the help of Mr. Masanori Sakai (an undergraduate school student from Kyoto University Faculty of Engineering), I collected 269 open-source antibody sequences from Protein Data Bank (PDB), including 169 entries for antibody Fv fragments (Fig. 4) and 100 entries for nanobodies (Fig. 5). The Fv sequences are aligned according to the Chothia numbering scheme and the frequency of amino acids at each position were calculated. As indicated by the red arrowheads in Fig.4 and Fig.5, there exist a few conserved residues at the boundary of CDRs. The amino acids at these sites are often tyrosine (Tyr or Y) residues which play dominant roles in mediating molecular contacts by forming hydrogen-bonding and cation-π interactions[41]. Although Tyr in the middle of CDRs is critical for the antigen-antibody interaction[42], the amino acids at these positions are located at the base of CDR loops and do not directly contact with antigens in many cases[43].

On the other hands, in the crystal structures of P20.1 Fv-clasp, 12CA5 Fv-clasp and NbALFA nanobody[14,20], I found that HCDR3 is surrounded by the amino acids mentioned above, namely H27 (27th amino acid of Fv heavy chain), H28, H32, H102, L32 (32nd amino acid of Fv light chain), L49 and L96 (Fig. 6). It has also been reported that these amino acids are frequently in contact with CDR residues[44]. Bulky residues at these sites might affect the affinity by modulating the flexibility of CDR loops and shaping them to the right conformation. Thus, I hypothesized that mutagenesis in these positions might affect the dissociation rate of antibodies without a significant sacrifice of specificity. In addition, H59 at the base of the HCDR2 loop was included among candidate sites (Fig. 7A). H59 is a conserved site that is also often occupied by Tyr.

To investigate whether mutagenesis at these sites could accelerate the dissociation rate and determine the amino acids for substitution, three candidate sites (H27, H59 and H102) at the base of each HCDR were selected for trial experiment. I performed site-directed mutagenesis on P20.1 Fv-EGFP by substituting each tyrosine residue for each of the other 19 amino acids (Fig. 7B). Almost all mutants specifically recognized TARGET tagged actin expressed in XTC cells. I therefore selected glycine (Gly or G) and alanine (Ala or A) as substitution residues, which could efficiently increase the

dissociation rate. By sequentially introducing site-directed mutagenesis into the candidate sites, the dissociation rates of Fv-EGFPs were increased by 2-99 folds (Fig. 7C). These mutants were used as IRIS imaging probes for epitope tags .

Furthermore, I examined whether the same strategy could be applied to nanobodies, because the frequency of amino acids at the candidate sites in nanobodies is similar to that in antibody V_H. I also included Nb37 into the candidate sites for mutagenesis in the nanobody because it is also a conserved Tyr residue in the vicinity of nanobody CDR1. I obtained three nanobodies from previous studies, namely NbALFA (anti-ALFA tag)[20], HS69 (anti-Homer)[21] and NV-Nb9 (anti-VGLUT)[22]. I fused EGFP to the C-terminus of the nanobody (Nb-EGFP) and purified it from the supernatants of transfected HEK293T cell cultures with the same methods as the production of Fv-EGFP. Multiple point mutations were collectively introduced into the nanobodies to efficiently increase the dissociation rates. Since the dissociation half-life of NbALFA is longer than 5.5 h, three Ala mutations at E53, R60 and V99 were also introduced to abolish several interactions with its antigen, according to a previous study[20]. The mutagenesis strategy also successfully increased the dissociation rate of nanobodies by orders of magnitudes (Fig. 7D). I also benchmarked the k_{off} of two nanobody probes against endogenous neuronal proteins, namely HS69^{H3} for Homer1 and NV-Nb9^{H4} for VGLUT, using primary cultured neurons. Both of the probe recognized the endogenous targets in neurons and exogenous proteins overexpressed in XTC cells and the dissociation rates were similar in each case.

The information of all Fv-EGFP and Nb-EGFP mutants generated in this study were summarized in Table 1. The Fig. 7C and 7D only show the mutants that were used as probes for successive IRIS imaging (hereafter called IRIS probes).

Section 3.5 Validation of new IRIS probes against epitope tags

The fidelity and specificity of my probes were validated using epitope tagged actin expressed in XTC cells. First, to estimate the specificity, the IRIS probes V302A^{H2L1}, 2H8^{H1L3}, P20.1^{H1L0}, 12CA5^{H6L2}, NbALFA^{H2} and S66B^{H1L0} was applied to permeabilized non-transfected XTC cells, respectively. The non-specific binding signals were negligible (Fig. 8A). In addition, compared with wild-type Fv-EGFPs, the non-specific signal did not increase after mutagenesis at candidate sites. Therefore, the point mutations at our candidate sites do not impair the specificity of the original antibodies (Fig. 8A and 8B).

I next performed super-resolution images of epitope tagged actin by the IRIS probes mentioned above. All of the IRIS probes against epitope tags, namely FLAG, TARGET, HA, V5, S and ALFA, clearly visualized actin bundles (Fig. 9A and 9B, representative image of FLAG-actin) with 45 nm in

FWHM (Fig. 9C) and resolved two actin bundles 60 nm apart (Fig. 9D). The resolution of actin filaments in Fig.9B is estimated to be 52.7 nm (Fig. 9G) using decorrelation analysis[32], which is similar to the FWHM value (45 nm). All five probes recognized the actin filaments of the same distribution and fidelity as previously reported Lifeact probe[6] (Fig. 9E and 9F, representative image of FLAG-actin).

Section 3.6 Multiplexed super-resolution imaging of focal adhesions

To demonstrate that the IRIS probes could be used for multiplex super-resolution imaging, I first examined the crosstalk between each epitopes by sequentially applying the IRIS probes to XTC cell that was individually transfected with HA, V5, S, FLAG, TARGET, or ALFA tagged actin (Fig.10). The crosstalk between targets is negligible in the single-molecule imaging. I then simultaneously transfected six epitope tagged proteins into XTC cells, including V5-actinin, ALFA-zyxin, S-histone2B (S-H2Bb), FLAG-vinculin, HA tagged myosin regulatory light chain 2 (HA-MRLC) and TARGET-paxillin. The ratio of plasmids for transfection was adjusted to 4:1:1:6:4:4 (weight) to balance the expression level. The probes were sequentially applied to the transfected XTC cell sample in the order of V302A^{H2L1}, Lifeact-Atto488, 2H8^{H1L3}, P20.1^{H1L0}, 12CA5^{H6L2}, NbALFA^{H2} and S66B^{H1L0}. All probes could be thoroughly washed away in the successive imaging procedure (Fig. 11A). In the reconstruction of multiplexed super-resolution imaging (Fig. 11B, 11C and 11D), V302A^{H2L1}, 2H8^{H1L3}, P20.1^{H1L0} and NbALFA^{H2} probes visualized the thick focal adhesion complex that associates with the tip of actin stress fibers. HA-MRLC is barely colocalized with focal adhesion complexes (Fig. 11D), which is consistent with previous immunostaining results[45]. HA-MRLC overlaps with F-actin in the cell center but was not observed near the cell edge (Fig. 11B). Moreover, an alternating pattern was visualized between V5-actinin and HA-MRLC along the actin arcs in the lamella of the cell (Fig. 11E), as reported in a previous study[46]. This alternative pattern on cell arcs is considered to participated in actin contraction and shortening[47]. Therefore, our probes were capable of visualizing multiple epitope-tagged components in a single cell, establishing a proof of principle for multiplexed super-resolution imaging of proteins for the targets without available antibodies.

Section 3.7 Validation of new IRIS probes against neuronal proteins

To verify the specificity of IRIS probes against endogenous proteins, I acquired super-resolution images with our new HS69^{H3} and NV-Nb9^{H4} probes in primary cultured neurons. The localization of Homer and VGLUT puncta detected by mutant probes overlapped with the staining pattern of wild-type nanobodies[21,22] (Fig. 12A). The specificity was also verified by a blank control (Fig. 12B) using non-transfected Hela cells, which express no VGLUT and very low levels of Homer[48]. Moreover, in

the neuron expressing mCherry-PSD95, which is the marker of post-synaptic density, the puncta detected by the HS69^{H3} probe overlapped with the signal for PSD95 (Fig. 12C). Pre-synaptic VGLUT visualized by the NV-Nb9^{H4} probe showed a clear pairing with dendritic spines marked by Lifeact (Fig. 12C). The periodic actin rings along an axon with ~190 nm periodicity[28] could be resolved by the Lifeact probe (Fig. 12D and 12E). These results indicated that IRIS probes against endogenous targets could finely localize the proteins at synapses.

Section 3.8 Multiplexed super-resolution imaging of neuronal proteins

I next performed multiplexed super-resolution imaging of endogenous proteins in primary cultured neurons (Fig. 13A). In addition to HS69^{H3}, NV-Nb9^{H4} and Lifeact, I used a new Fv-EGFP derived from an L8/15 antibody against Snapin[49]. Snapin is a protein involved in neurotransmission and endosome trafficking[50,51]. The dissociation rate of wild-type L8/15 is fast enough (0.519 s^{-1}) to be used as an IRIS probe. Neurons were infected with adeno-associated virus (AAV) carrying mCherry cDNA to visualize the morphology of neuron (Fig. 13A). Images of four targets were sequentially acquired in the order of F-actin, VGLUT, Snapin and Homer (Fig. 13A-G). I was able to observe clear separation between pre-synaptic VGLUT puncta, post-synaptic actin and the scaffold protein Homer (Fig 13C-G). F-actin was highly concentrated at the dendritic spines (Fig. 13E and 13F). Post-synaptic actin was located at the base of Homer-associated structures (Fig. 13E and 13F) and occasionally formed a cage-like structure surrounding Homer (Fig. 13D and 13F) as described previously[52]. Snapin distributed ubiquitously in neurons (Fig. 13B and 13C) and overlapped with VGLUT puncta (Fig. 13E).

In IRIS super-resolution microscopy, one label refers to a binding (on-off) events of an IRIS probe. The label number of VGLUT and Homer puncta in mature synapse are 3,798 ± 945 and 694 ± 269 (mean ± SD), respectively (Fig. 13H). The number of VGLUT 1/2 and Homer 1b/c molecules in a synapse are reported to be 8,254 [53] and 233 [54]. Based on these numbers, I estimate that approximately 95% of Homer and 37% of VGLUT molecules are labelled at least once. Tiny Homer clusters (~0.1 μm) paired with VGLUT are visualized by IRIS probes with 155 labels (Fig. 13G).

Section 3.9 Advantages of IRIS over other SMLM techniques

In conventional multiplexed SMLM, the labeling density might be deteriorated by poor accessibility of antibodies in a confined imaging area (see the cartoon in Fig. 14 for illustration). I next examined whether staining with multiple antibodies could impair the accessibility of another antibody probes in the tiny spines. IRIS images of Homer were acquired using nanobody probe HS69^{H3} before and after antibody incubation as schemed in Fig. 15A. The targets of primary

antibodies are GKAP, SHANK3 and PSD95, which exist in close proximity of Homer[55,56]. The label number of Homer probes in each punctum was counted before and after antibody incubation. In the samples which were incubated with both primary antibodies and secondary antibodies, a significant part of signals (~32%) in Homer puncta were lost (Fig. 15B and 15C). The label numbers did not decrease in the samples that were incubated only with secondary antibodies (Fig. 15B and 15C). These results indicate that interference between antibodies may impair the accessibility of each probe and lead to sparse labelling problem in conventional multiplexed SMLM approaches.

In addition, I directly compared IRIS with DNA-based point accumulation for imaging in nanoscale topography (DNA-PAINT) and Direct stochastic optical reconstruction microscopy (dSTORM)[57] by sequentially performing super-resolution imaging on Homer or VGLUT in the same neuron samples (Figure 15D and 15E). In STORM and PAINT images, many pixels within the puncta are lack of labels. I also compared an IRIS image of synapse (Fig. 15B, upper left) with published images of STORM[55] and DNA-PAINT[58] (Fig. 16A). Although I cannot assert which pattern reflects the real distribution of the molecules, IRIS appears to show more continuous labelling than other methods. I further compared the label density and distribution between IRIS and STORM images according to the previous method[55]. IRIS achieved ~4 folds higher label density than STORM (Fig. 16B). Importantly, multiple localization points may arise from repeated detection of a single label in STORM and DNA-PAINT. IRIS probes generated by my approach have the potential to super-resolve multiple endogenous targets of interest with high labelling density.

Chapter 4 Discussion

In this research, I showed that IRIS could overcome the interference between multiple antibodies in a confined area and the resultant scarce labelling, which has been an intrinsic problem of super-resolution microscopy[6,59]. Besides IRIS, other super-resolution approaches such as Exchange-PAINT[60-63] and sequential elution-staining STORM (maSTORM)[62] could achieve highly multiplexed imaging in a single biological sample. Single fluorophore could also be used in these methods to prevent chromatic aberration. MaSTORM exchanges the antibodies by harsh elution and bleaching steps, which probably do cumulative damage to the sample across multiple rounds of imaging[62]. By contrast, fluorescent probes in IRIS and Exchange-PAINT could be easily washed out by moderate buffers without high salt concentration and harsh pH. The sample preparation of IRIS is simple because it does not require any antibody incubation steps. Similar to DNA-PAINT, IRIS does not suffer from photobleaching, which enables longer imaging duration and achieve higher resolution. In addition, it has been reported that chaotropic reagent KSCN can increase the dissociation rate of 12CA5 antibody by several folds[64]. However, the dissociation rate of 12CA5 accelerated by KSCN is still 250-fold lower than the dissociation rate of $12CA5^{H6L2}$ mutant. This low dissociation rate led to an extremely long imaging time in their PAINT super-resolution microscopy.

I have developed two kinds of antibody-based IRIS probes: Fab probes[8] and recombinant probes. Although Fab probe has to be screened from numerous hybridoma clones through many validation steps[8], it is suitable for observation target without existing antibody. The screening and validation process of recombinant probe is much simpler than Fab probe. It only requires mutagenesis on the off-the-shelf antibodies regardless of whether the structure is known. The specificity of each antibody-based IRIS probe was validated by comparing the super-resolution images with a positive marker, or the staining pattern of the original antibody fragments. Noise of each probe was also measured by the densities of non-specific binding in non-transfected cell controls (typically, ~1% of the total signal in transfected cells). The quantitative assessment based on single-molecule binding enabled specificity validation of the low-affinity binders.

As a practical consideration in the mutagenesis strategy of recombinant probes, I mainly used Ala substitution because mutants with Gly substitutions at the same candidate sites sometimes deteriorate the antigen recognition. Point mutations at H/Nb27, H/Nb28 and Nb37 could be frequently introduced without disrupting antigen recognition. Mutations at H/Nb32, H/Nb59, L32, L49 and L96 occasionally led to the loss of antigen recognition, although the k_{off} value could be effectively increased by mutagenesis in these sites. Mutagenesis in H/Nb102 may be less effective than the other sites. Combination of point mutations further increases the dissociation rate and retains the binding specificity with a high probability. Multiple point mutations can be introduced collectively to improve the efficiency. Dozens of recombinant-antibody-based IRIS probes were generated by Ala or Gly

substitutions at candidate sites. It typically costs 2-4 weeks to generate a new IRIS probe from an existing antibody sequence. Based on the sequence information in the antibody database, such as Protein Data Bank (PDB)[65] and ABCD database[66], a large repertoire of proteins can be subjected to super-resolution analysis using IRIS multiplex super-resolution microscopy.

The candidate sites for mutagenesis in this study is interesting because all of them are at the boundary between CDR and FR. I avoided modifying the residues in the middle of CDRs because they are considered critical for the antigen recognition[67-69]. Another reason is that mutation sites for each antibody have to be explored individually when no structure information is available owing to the high diversity of the CDR sequences. On the other hand, candidate sites in this study are conserved in most antibodies, where Ala or Gly substitution could effectively increase the dissociation rate of antibodies. IRIS probes generated by my mutagenesis strategy still retain their specificity, probably because the mutation sites do not contact with the antigens in many cases[43] and the paratope have been well preserved.

Limitations of the study

- Although the database for antibodies is expanding rapidly, the sequence information of existing antibodies is not always disclosed, making it difficult to develop recombinant IRIS probes for the targets without available antibody sequences.
- The dissociation rate of mutants increased by ~100-fold in this study. For high-affinity antibodies with koff smaller than 10^{-4} s^{-1}, such as NbALFA, it might be necessary to modify additional antigen-binding sites in the middle of CDR loops to further increase the dissociation rate, which would require the information of cocrystal structures.
- When using the IRIS probes against overexpressed proteins, the expression level of targets must be estimated empirically by acquiring 1,000–2,000 frames.

Chapter 5 Conclusion

In summary, I have developed a versatile site-directed mutagenesis strategy to accelerate the dissociation rate of antibodies and generate a series of validated fast-dissociating antibody fragments. These recombinant fragments are especially suited for multitarget super-resolution imaging. Potential applications of these fragments also include multiplexed immunostaining, cell typing/sorting, western blotting and so on. The pipeline I established can be used in generating fast-dissociating antibodies efficiently from numerous resources of off-the shelf antibodies.

Figures and Tables

Fig. 1 Multiplexed super-resolution imaging of cell and tissue by Fab probes

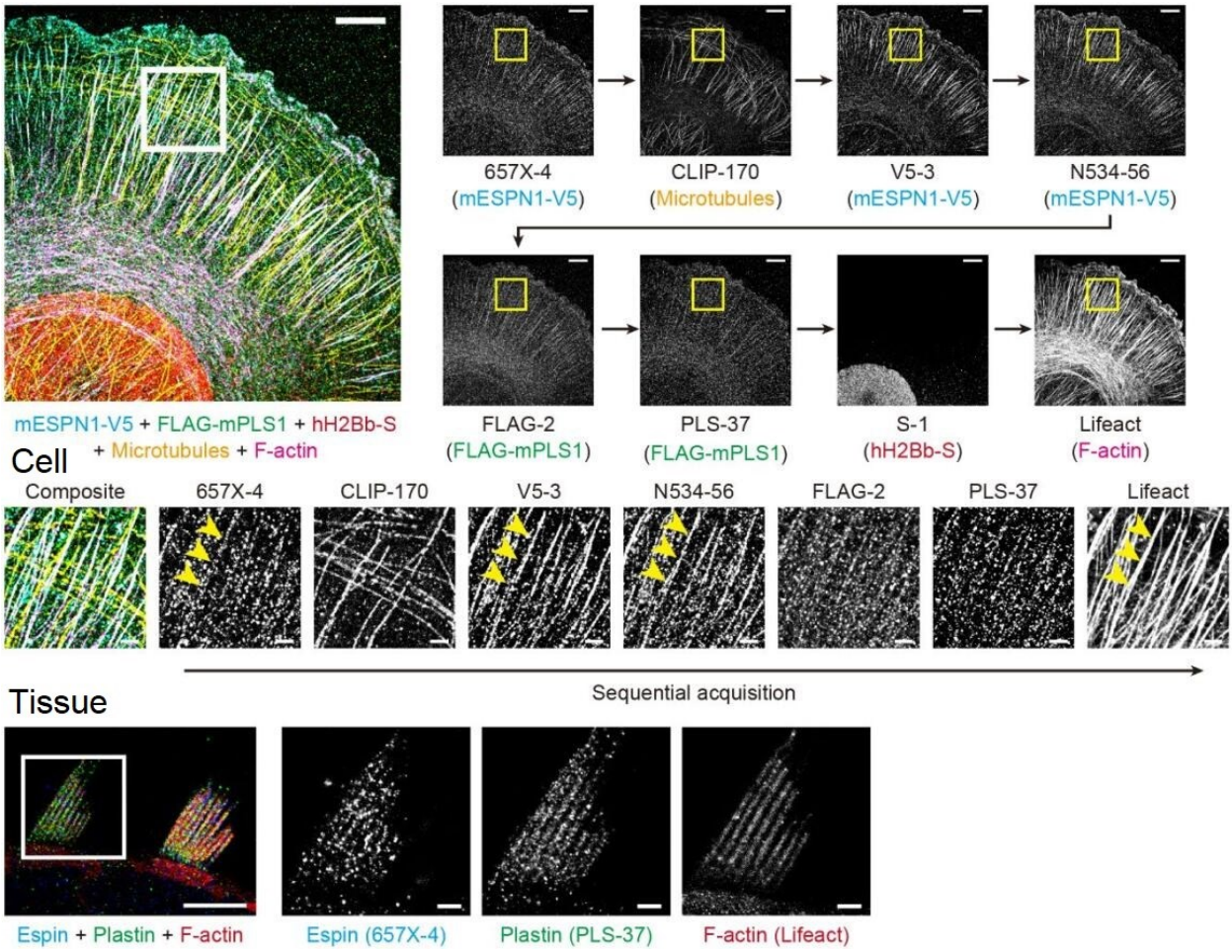

Sequential IRIS imaging of proteins overexpressed in XTC cell and endogenous proteins in inner ear tissue by Fab probes. Scales bars, 5 μm for full-clip cell, 1 μm for enlarged cell, 5 μm for full-clip tissue and 1 μm for enlarged tissue. The figure was reproduced from the Figure S9 of the reference[8].

Fig. 2 Construction of recombinant IRIS probe

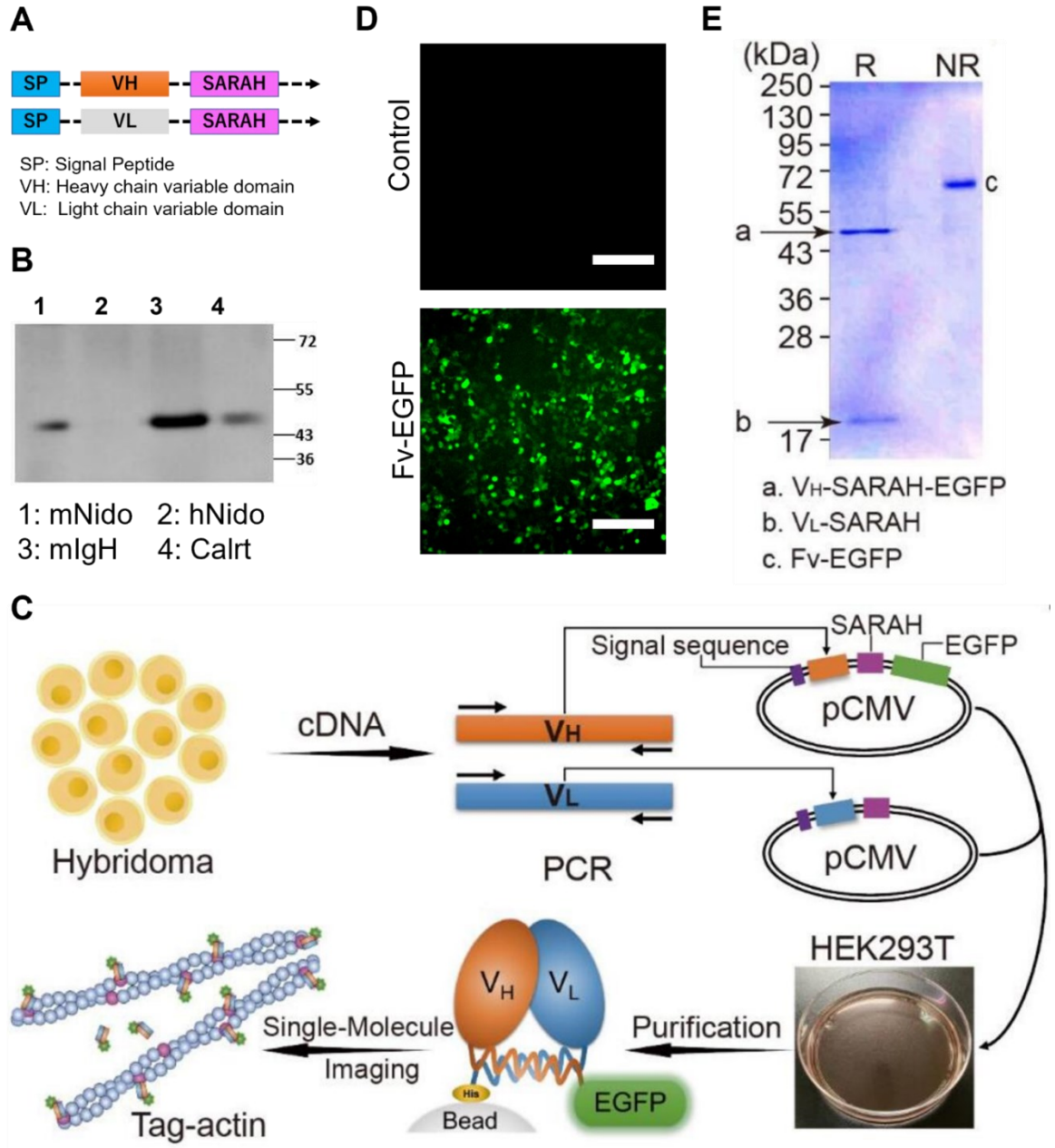

(A) Construction of Fv-clasp. Pink segment shows the SARAH domain of human Mst1 kinase.

(B) Comparison of the yield of Fv-clasp which was expressed and secreted using different signal peptides.

(C) Diagram of Fv-EGFP generation.

(D) Fv-EGFP expressed in small scaled cultured HEK293T cells. Non-transfected cells were used as control group. Scale Bars, 20μm.

(E) The SDS-PAGE profile of the purified P20.1 (anti-TARGET tag) Fv-EGFP under reducing (R) and non-reducing (NR) conditions.

Fig. 3 Determination of the dissociation rate

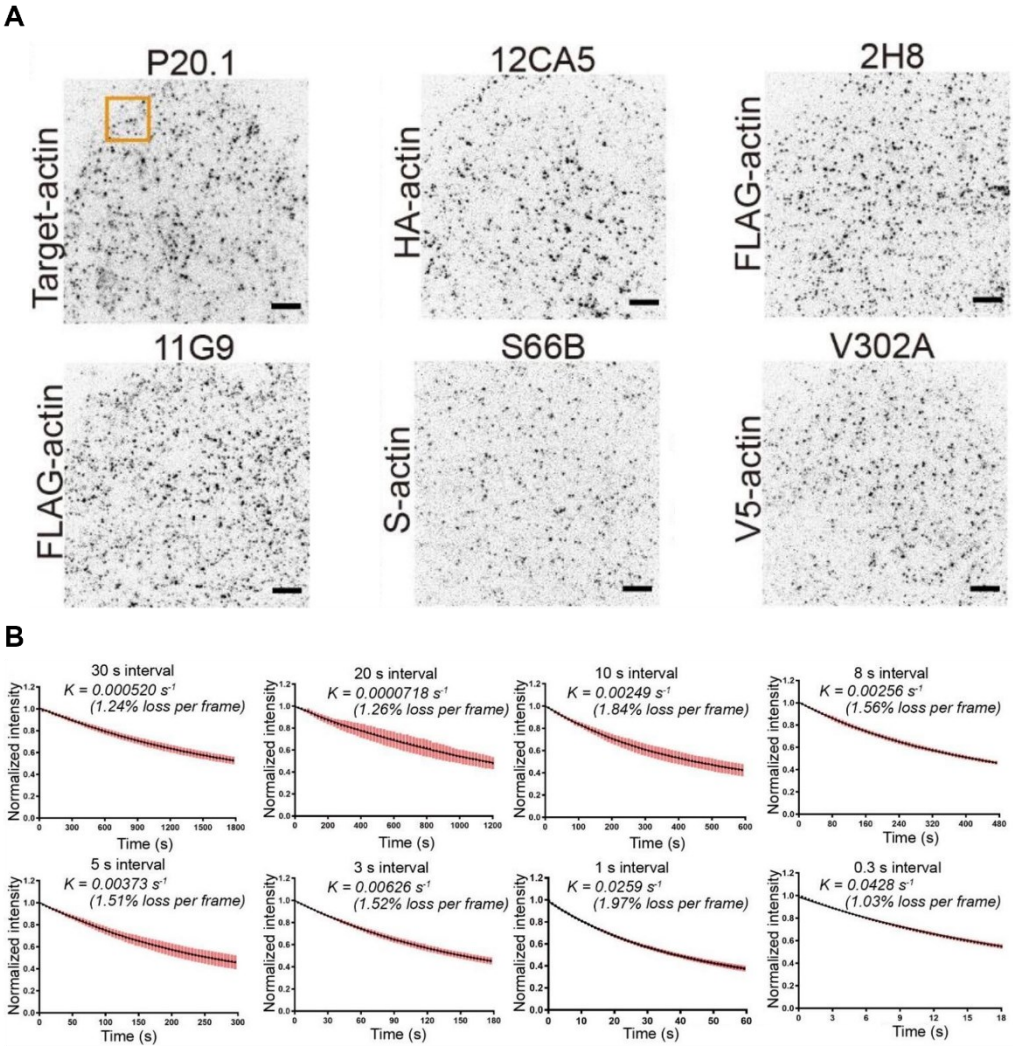

C

Fv-EGFP (Wild type)	Time-lapse interval (s)	Best-fit values			R^2	Total spot number of regression		
		Y0	Half-life* (s)	k_{off}* (1/s)		1	2	3
P20.1 (TARGET)†	8	0.9196	21.0	3.30×10^{-2}	0.9607	694	1007	1019
12CA5 (HA)†	20	0.8688	112	6.21×10^{-3}	0.9657	655	654	699
2H8 (FLAG)	20	0.8871	91.1	8.03×10^{-3}	0.9787	546	624	523
11G9 (FLAG)	0.3	0.8867	1.78	3.90×10^{-1}	0.9765	805	1261	898
S66B (S)	1	0.8706	4.97	1.39×10^{-1}	0.9630	411	528	492
V302A (V5)	3	0.8244	21.5	3.22×10^{-2}	0.9568	680	657	948

(A) Single-molecule imaging of Fv-EGFPs (WT) bound to the corresponding epitope-tagged actin expressed in XTC cells. The probes were applied at a very low concentration (0.05 nM - 0.1nM) to perform the single-molecule imaging. Scale bar, 5 μm.

(B) The photobleaching rate of EGFP measured using XTC cells expressing EGFP-actin. Cells were fixed with 3.7% PFA in cytoskeleton buffer containing 0.5% Triton-X100. Time-lapse images were acquired under the same exposure condition as the k_{off} determination. Red bars indicate SD.

(C) Dissociation rate of wild type Fv-EGFPs fitting by one phase decay model. The half-life ($T_{1/2}$) is the time needed to let dissociate half of the probes from the targets. It is calculated as $T_{1/2} = \ln 2 / k_{off}$.

Fig. 4 Frequency of amino acid in antibody variable region

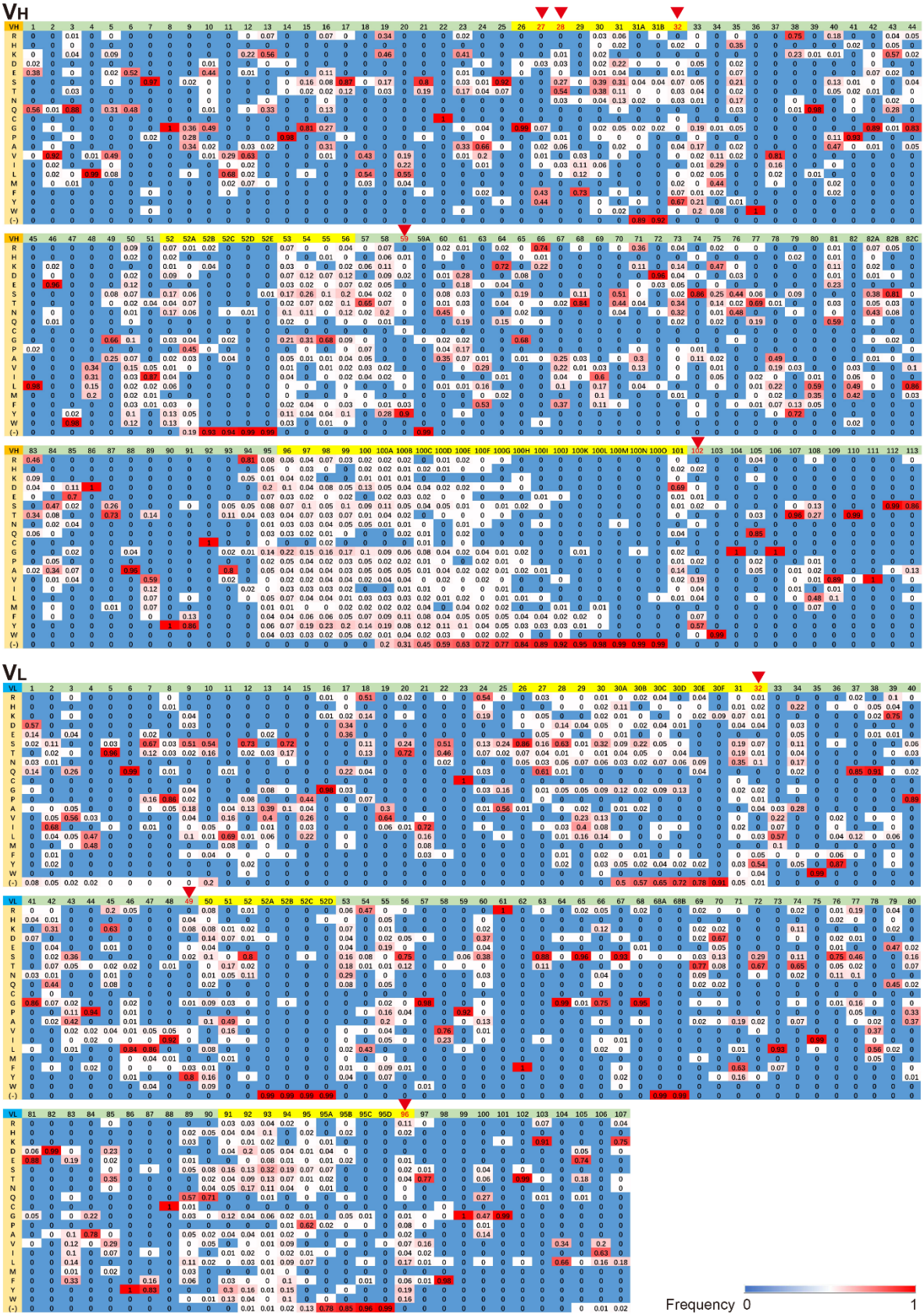

Alignment of 169 antibody sequences collected from PDB, following the Chothia numbering scheme. Frequencies of amino acids (one letter) at each position are shown in the heatmap. CDR regions are annotated in yellow according to the Chothia definition. Red triangles and red numbers indicate

candidate positions for mutagenesis at the base of CDR loops. Note that the candidate residues are conserved in most antibodies. The data collection was supported by Mr. Masanori Sakai, who is one of the co-authors of the basis article.

Fig. 5 Frequency of amino acid in nanobodies

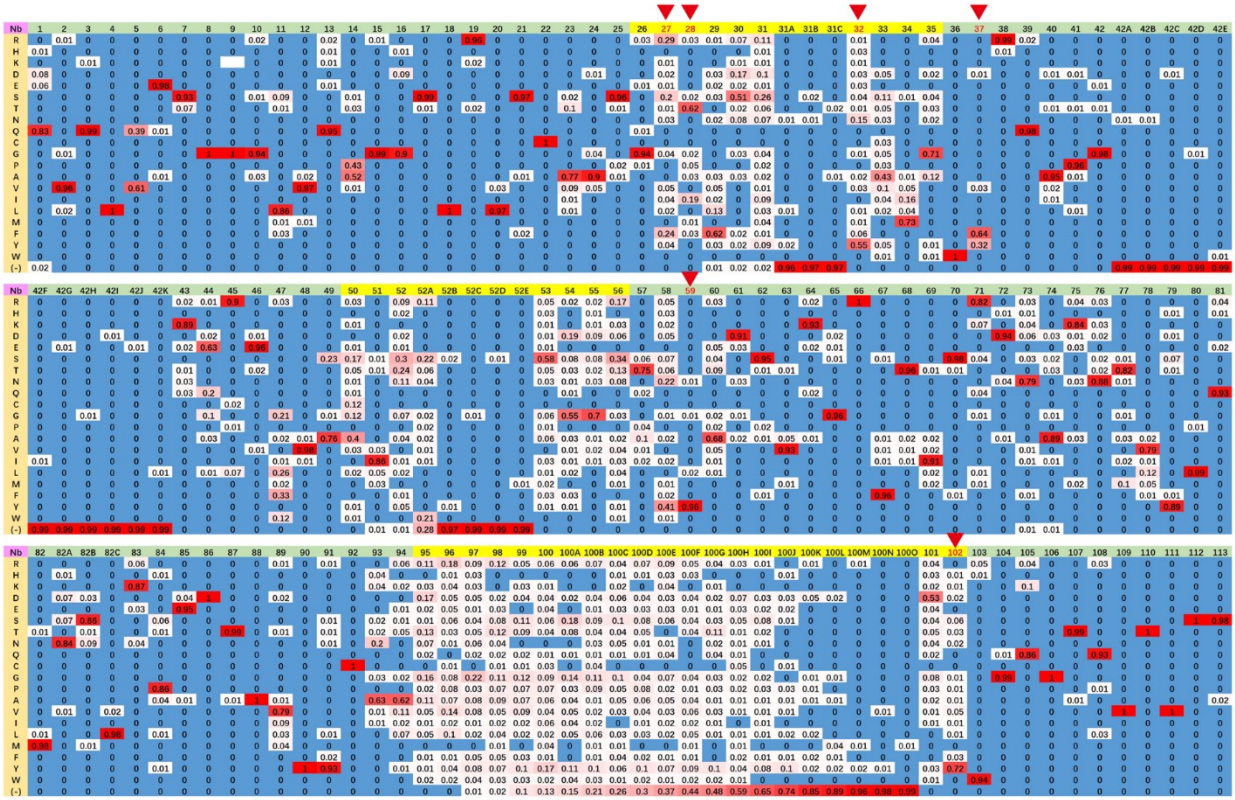

Alignment of 100 nanobody sequences acquired from PDB, following the Chothia numbering scheme. Frequencies of amino acids at each position are shown in the heatmap. CDR regions are defined as described previously[26]. Red triangles and red numbers indicate candidate positions for mutagenesis in nanobodies. The data collection was supported by Mr. Masanori Sakai, who is one of the co-authors of the basis article.

Fig. 6 Candidate mutation sites in the co-crystal structures

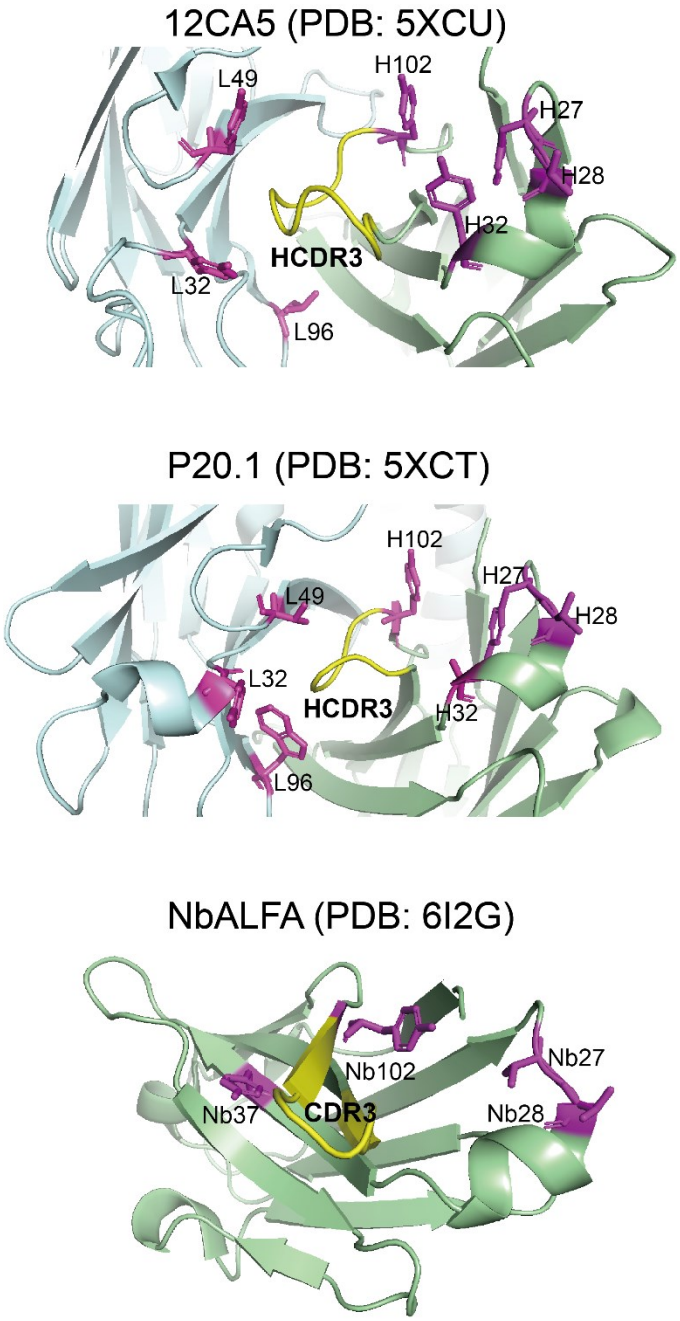

Illustration of candidate sites (magenta) surrounding HCDR3 (yellow) in P20.1 Fv-clasp (PDB: 5XCT), 12CA5 Fv-clasp (PDB: 5XCU) and NbALFA (PDB: 6I2G). V_H (or nanobody) and V_L are colored in green and blue, respectively

Fig. 7 Candidate sites for mutagenesis in Fv fragment and nanobody

A

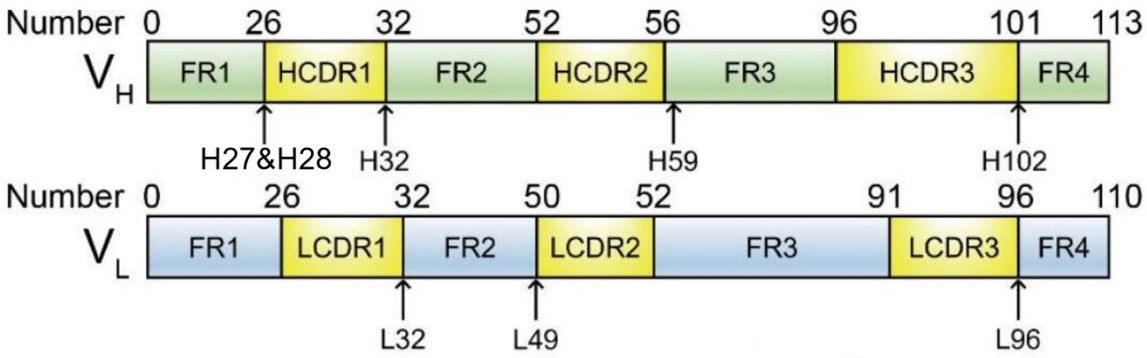

B

P20.1 V_H	Gly(G)	Val(V)	Ser(S)	Asp(D)	Cys(C)	Gln(Q)	Ala(A)	Trp(W)	Ile(I)	Pro(P)	Glu(E)	Leu(L)	Asn(N)	Met(M)	Thr(T)	His(H)	Arg(R)	Phe(F)	Lys(K)
HY27	2.89	3.38	3.78	3.11	3.53	4.34	2.72	6.21	4.10	3.98	2.37	8.18	6.28	7.00	8.98	8.09	6.96	13.40	X
HY59	2.09	5.62	5.12	4.60	7.36	3.18	7.03	4.70	7.11	11.01	8.70	6.70	7.05	7.53	7.80	7.26	9.16	14.45	11.02
HY102	5.01	2.61	3.15	8.02	6.76	8.87	7.70	7.75	8.32	X	11.39	8.45	10.41	9.78	7.65	8.35	7.60	10.30	23.04

C

IRIS probe (Clone$^{\text{mutant code}}$)	Epitope tag	Mutation site 1	Mutation site 2	Mutation site 3	Mutant koff (1/s)	Mutant half-life (s)	WT half-life (s)
P20.1^{H1L0}	TARGET	HY59G			0.332	2.09	21.0
12CA5^{H6L2}	HA	HT28A	HY32A	LY49A	0.601	1.15	112
2H8^{H1L3}	FLAG	HS28A	LY96A		0.407	1.70	91.1
V302A^{H2L1}	V5	HY27G	LY32A		0.567	1.22	21.5
S66B^{H1L0}	S	HS28A			0.276	2.51	4.97

D

IRIS probe (Clone$^{\text{mutant code}}$)	Antigen	Mutation site 1	Mutation site 2	Mutation site 3	Mutation site 4	Mutation site 5	Mutation site 6	Mutant Half-life (s)	Mutant k_{off} (1/s)	WT k_{off} (1/s)
NbALFA^{H2}	ALFA tag	V27G	T28A	Y37A	E53A	R60A	V99A	2.10	3.31×10^{-1}	$<3.48 \times 10^{-5}$
HS69^{H3}	Homer	S27G	T28A	F37A	Y59A			7.13	9.71×10^{-2}	8.97×10^{-4}
NV-Nb9^{H4}	VGLUT	R27G	T28A	Y32A	F37A	Y102A		7.14	9.32×10^{-2}	1.64×10^{-3}

(A) Illustration of the candidate sites for point mutation in Fv region.

(B) Half-lives of P20.1 Fv-EGFP (anti-TARGET tag) single-point mutants at the base of HCDR1 (HY27), HCDR2 (HY59) and HCDR3 (HY102). Mutants that did not recognized the TARGET-actin expressed in XTC cells are annotated in gray and letter "X".

(C) Summary of mutation sites and dissociation rates of mutant Fv-EGFPs, which were used as fast-dissociating IRIS probes in this paper.

(D) Summary of mutation sites and dissociation rates of mutant Nb-EGFPs, which were used as fast-dissociating IRIS probes in this paper.

Fig. 8 Validation of new IRIS probes against epitope tags

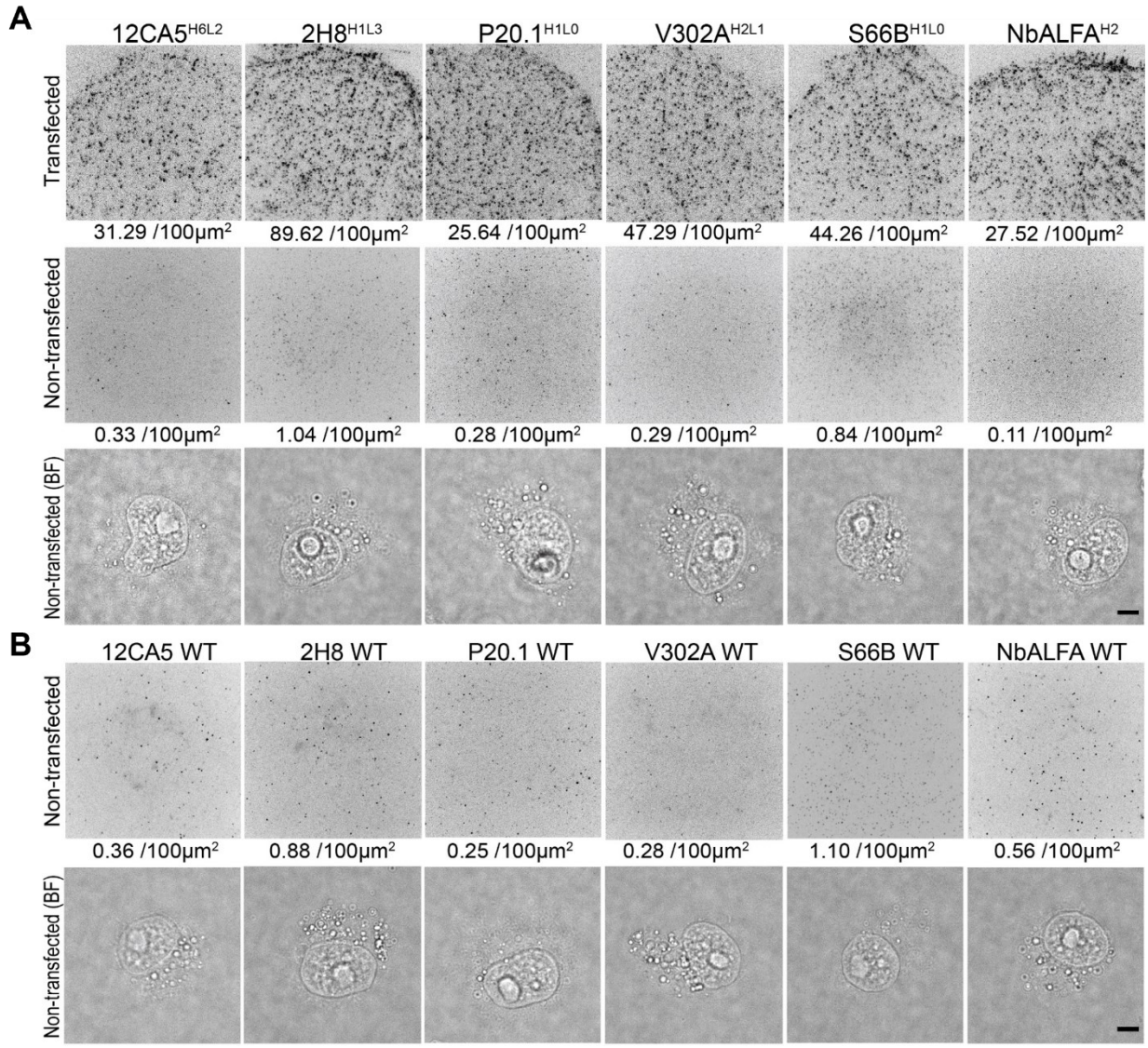

(A) Negative control of epitope tag probes using non-transfected XTC cells. Probes were applied at 1 nM, and images were acquired under the same conditions used in super-resolution imaging in Fig. 9. One frame of single-molecule images used for super-resolution reconstruction in Fig. 9 are shown in top row for comparison. Maximum projections of 500 frames acquired every 100 ms from non-transfected XTC cells are shown in the middle row. Bright field (BF) images of the same non-transfected XTC cells are shown in the bottom row. Spot density per frame is shown beneath each image (average density of 500 single-molecule frames for each panel). Scale bars, 5 μm.

(B) Negative control of wild type Fv-EGFPs and Nb-EGFPs using non-transfected XTC cells. Probes were applied at 1 nM, and images were acquired under the same conditions as in **(A)**. Maximum projections of 500 frames acquired every 100 ms from non-transfected XTC cells are shown in the top row. BF images of the same non-transfected XTC cells are shown in the bottom row. Spot density per frame is shown beneath each image (average of 500 frames). Scale bars, 5 μm.

Fig. 9 Super-resolution imaging of epitope tagged actin in XTC cells

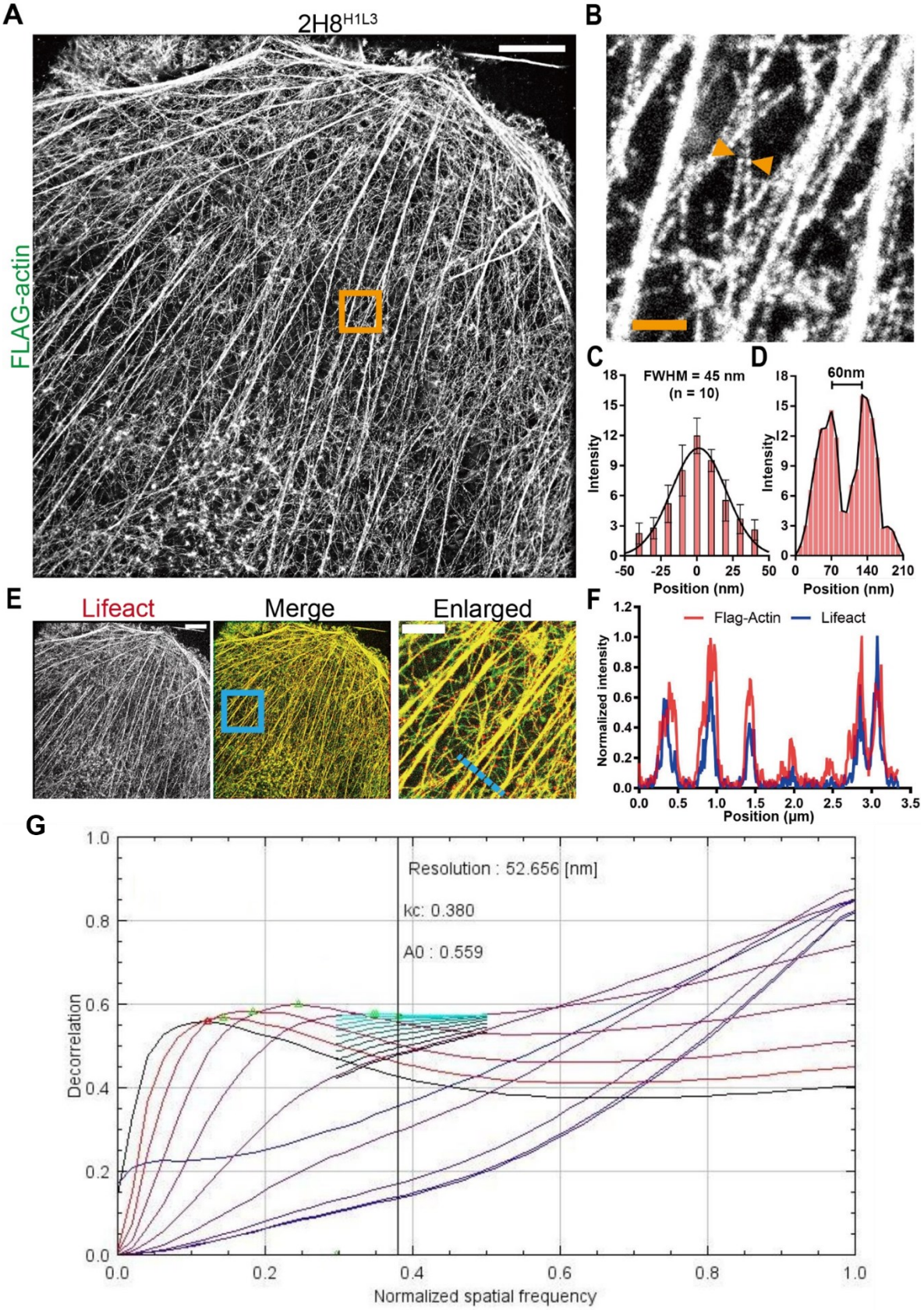

(A) Super-resolution images of FLAG-actin expressed in XTC cells using the 2H8^{H1L3}. Scale bar, 5 μm.

(B) The enlarged image of the orange box in **(A)**. Decorrelation resolution, 52.7 nm. Scale bar, 500 nm.

(C) Cross-sectional profile of actin bundles (n = 10) aligned by the center of each bundle. The line shows a Gaussian fit with FWHM of 45 nm. Error bars represent SD.

(D) Cross-sectional profiles for two nearby actin bundles between the arrowheads in **(B)**.

(E) Super-resolved actin imaged with Lifeact Atto-488 after washing away the probe in **(A)**. FLAG-actin (green) in **(A)** and Lifeact image (red) are shown in the merged image. Scale bar, 5 μm for full-scale images and 2.5 μm for the enlarged image.

(F) Cross-sectional profile of actin filaments across the blue dotted line in **(E)**.

(G) Decorrelation analysis of image in panel **(B)** using ImageJ plugin provided by Descloux et al[32].

Fig. 10 Examination of crosstalk between probes against epitope tags

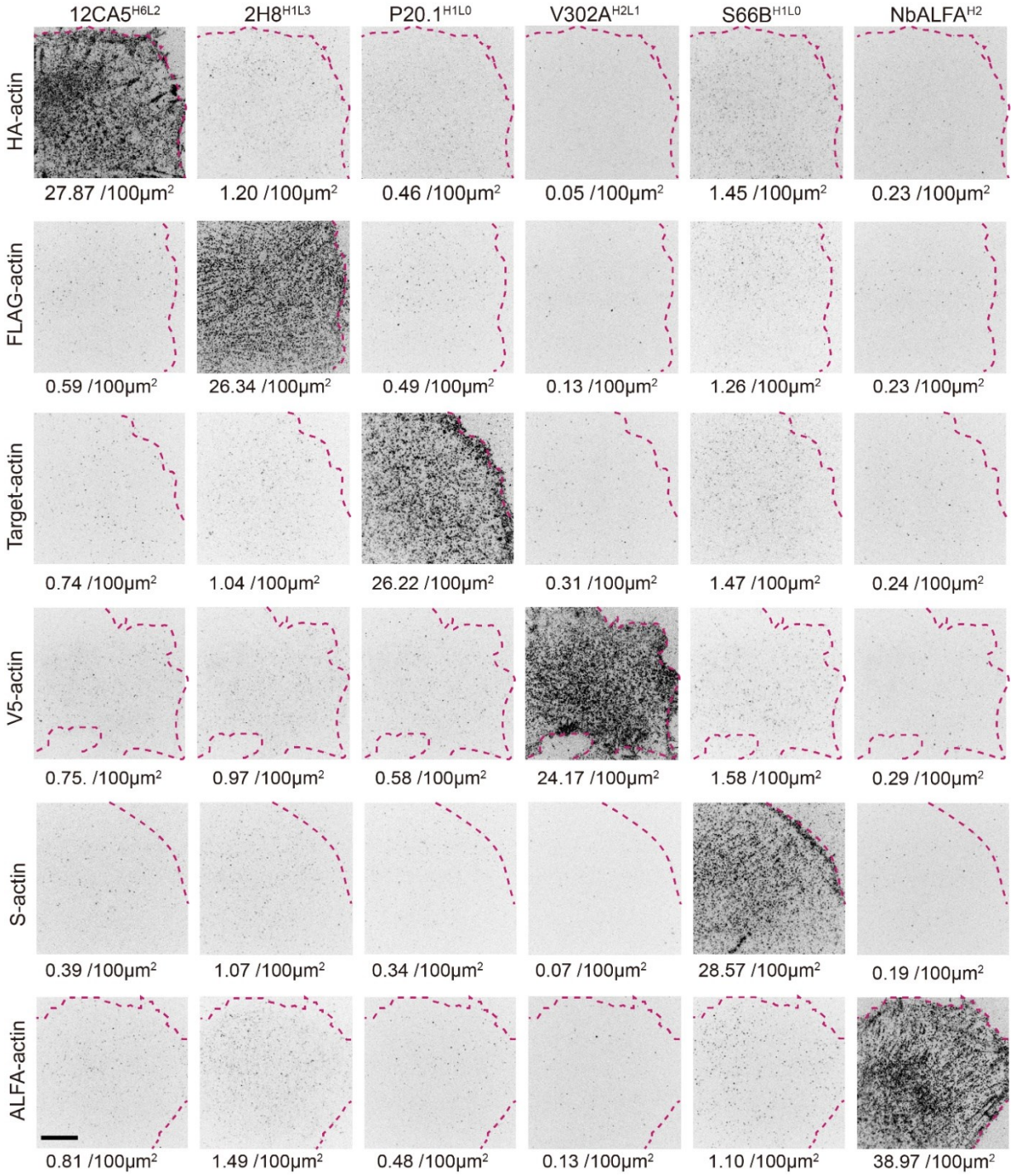

Examination of crosstalk between each probe against epitope tag. Antibody probes (1 nM) against epitope tags were sequentially applied to the XTC cells which were individually transfected with HA-actin, FLAG-actin, TARGET-actin, V5-actin, S-actin or ALFA-actin. Each sample was washed 8 times with PBS between successive probes. Each panel shows the maximum projection of 500 single-molecule frames acquired every 100 ms. Spot density per frame is shown beneath each panel (average of 500 frames). Scale bar, 10 μm.

Fig. 11 Multiplexed super-resolution imaging of epitope tagged focal adhesions in XTC cells

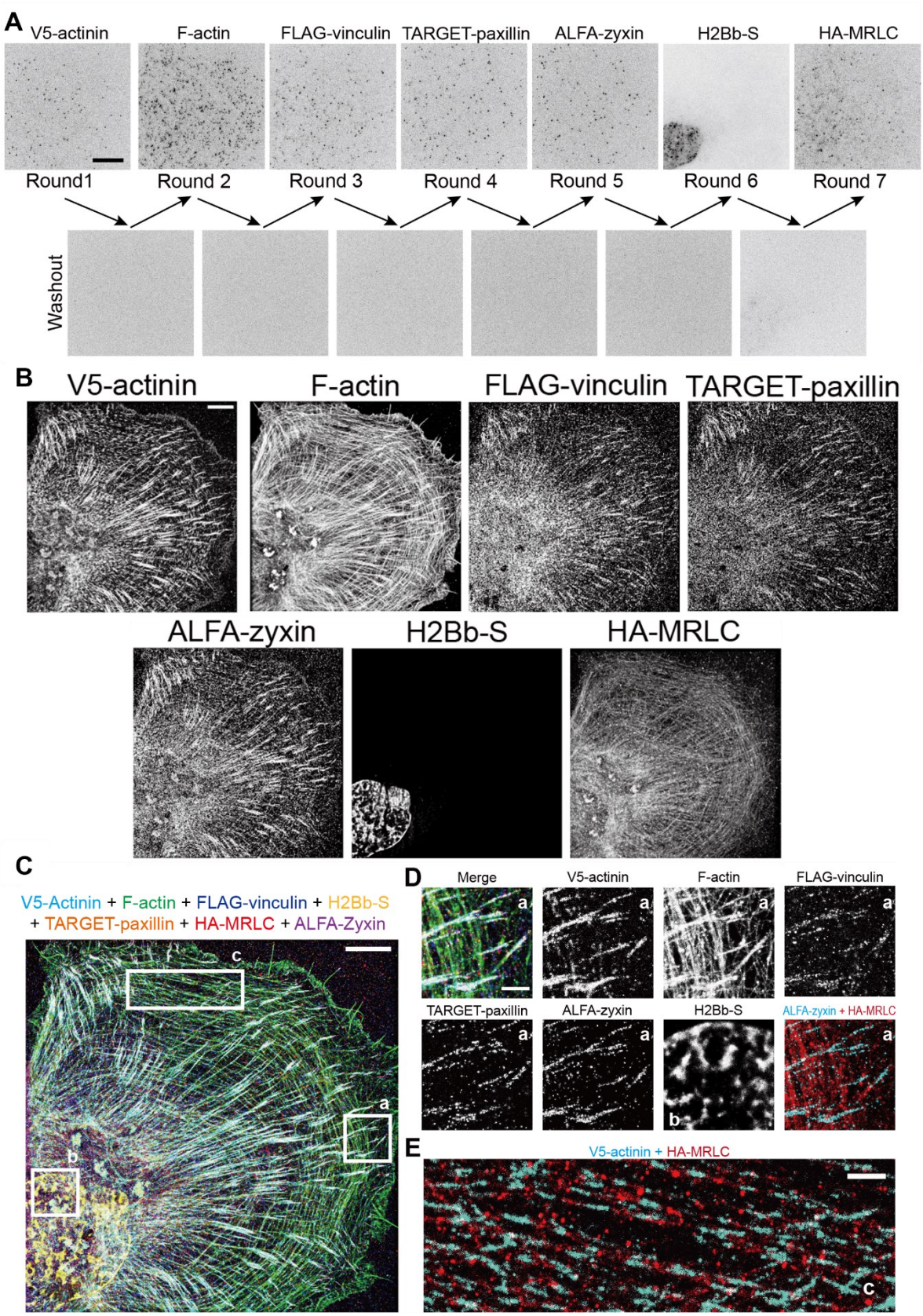

(A) Single-molecule imaging of six epitope tagged proteins expressed in XTC cells. Image stacks were sequentially acquired using V302A^{H2L1}, Lifeact, 2H8^{H1L3}, P20.1^{H1L0}, NbALFA^{H2}, S66B^{H1L0} and

12CA5^{H6L2}. Each successive probe was applied to the sample after washing out the preceding probe with PBS. Scale bar, 10 μm.

(B) Super-resolution images were reconstructed from V5-actinin, F-actin, FLAG-vinculin, TARGET-paxillin, ALFA-zyxin, H2Bb-S and HA-MRLC of single-molecule images. Scale bar, 5 μm.

(C) Seven-color IRIS image of six epitope-tagged proteins and endogenous F-actin in a single XTC cell. Scale bar, 5 μm.

(D) The enlarged images of boxed regions a and b in **(C)**. Scale bar, 1 μm.

(E) The enlarged images of V5-actinin (cyan) and HA-MRLC (red) along actin arcs in the lamella region (box c) in **(C)**. Scale bar, 1 μm.

Fig. 12 Validation of the IRIS probes against neuronal proteins.

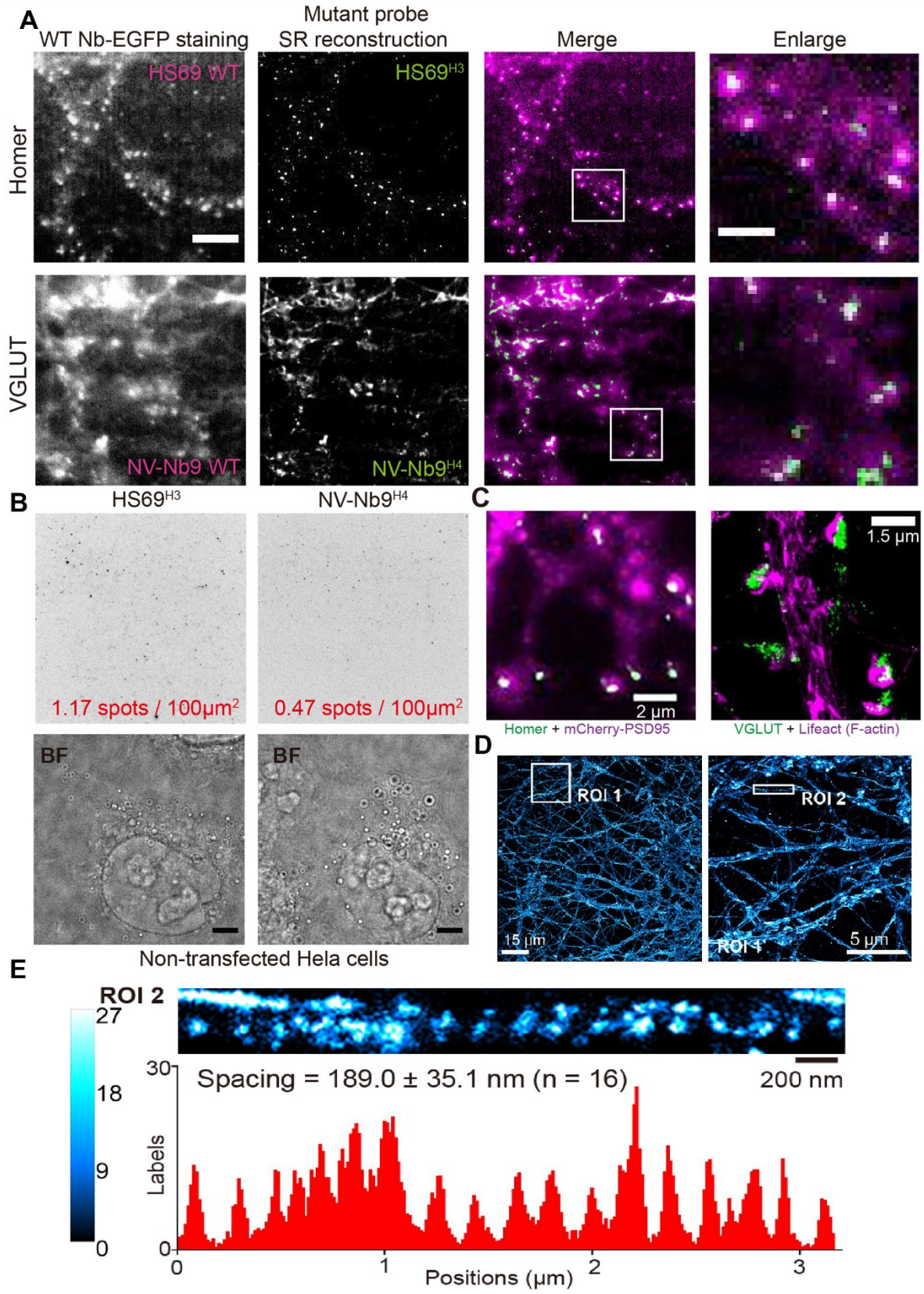

(A) Specificity validation of Homer and VGLUT probes by visualizing colocalization of puncta in primary cultured neurons (DIV 45). Super-resolution images were reconstructed from 15,000 frames using Homer probe (1 nM) and 40,000 frames using VGLUT probe (1 nM), respectively, followed by

washout and staining with WT Nb-EGFP. Scale bars, 5 μm for full-clip images and 1.5 μm for enlarged images.

(B) Validation of the nanobody probe specificity by applying them (2 nM) to non-transfected Hela cells. Images are maximum projections of 500 frames acquired every 100 ms. Spot density per frame is shown in each panel (average of 500 frames). Nanobody probes, 2 nM. Scale bars, 5 μm.

(C) Evaluating the specificity of neuronal protein probes by comparing the distribution with a positive marker. Puncta visualized by $HS69^{H3}$ (super-resolution image) colocalized with overexpressed mCherry-PSD95. Pre-synaptic VGLUT (green) signals visualized by the $NV\text{-}Nb9^{H4}$ probe were paired with post-synaptic actin (magenta), which is the super-resolution image obtained with the Lifeact probe.

(D) and (E) Super-resolution image of axonal actin rings in primary cultured neurons (DIV28) using Lifeact-Atto550 probe. **(E)** is the enlarged image of ROI 2 in **(D)**. The position of labels (average) is projected to one dimension along the axon long axis (bottom of ROI 2). The average spacing of actin rings and the SD value are shown in the panel (n = 16). Calibration bars show the number of labels in each pixel (13.5 nm in length)

Fig. 13 Multiplexed super-resolution imaging of primary neuron

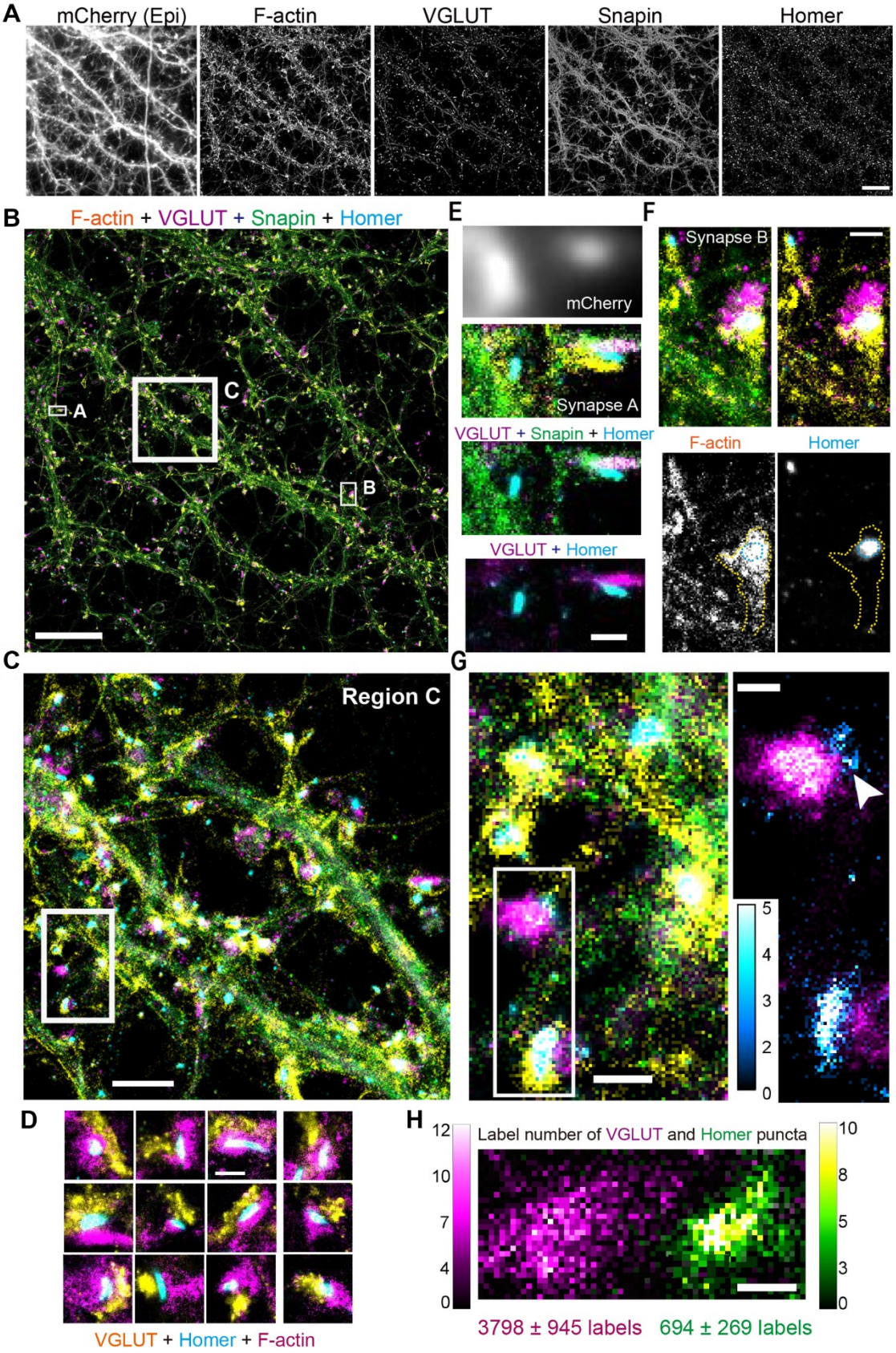

(A) Super-resolution images of F-actin (Lifeact), VGLUT, Snapin and Homer in primary cultured neurons. An overall image of the neuron was acquired using overexpressed free mCherry by epi-fluorescence. Scale bars, 10 μm.

(B) Multiplex imaging, merging four super-resolution images in **(A)**. Scale bars, 10 μm.

(C) Enlarged images of boxed region c in **(B)**. Scale bars, 2 μm.

(D) Gallery of 12 enlarged synapses found in **(B)**. Scale bars, 500 nm.

(E) and (F) Enlarged images of boxed synapses A and B in **(B)**. Yellow and cyan dotted lines show the shape of the spine and the position of the Homer, respectively. Scale bars, 500 nm.

(G) Enlarged images of boxed region in **(C)**. A small homer cluster (~0.1 μm) was indicated by the white arrowhead in the right panel with 155 labels (one "label" refers to a binding event of IRIS probe to target protein). Only VGLUT (magenta) and Homer (cyan) clusters are shown in the right panel. Calibration bar shows the number of labels in each pixel (13.5 nm in length). Scale bars, 500 nm (left panel) and 200 nm (right panel).

(H) Label number of VGLUT (magenta) and Homer (green) in a synapse found in **(B)**. Calibration bars show the number of labels in each pixel (13.5 nm in length). Average label numbers in ten VGLUT or Homer puncta and SD were shown beneath the image. Scale bar, 200 nm.

Fig. 14 Illustration of the spatial interference in conventional SMLM

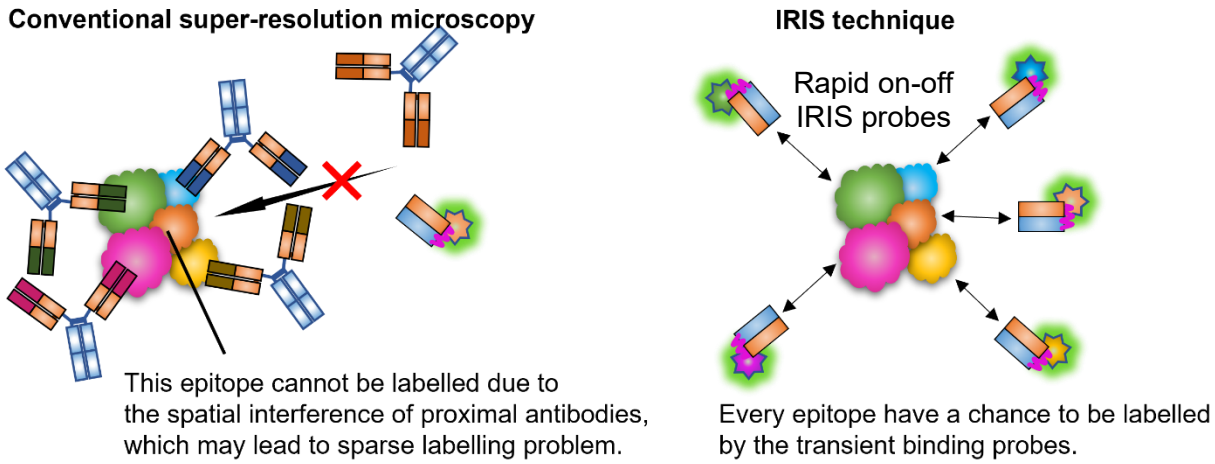

Fig. 15 Interference between antibodies cause deteriorated labeling density

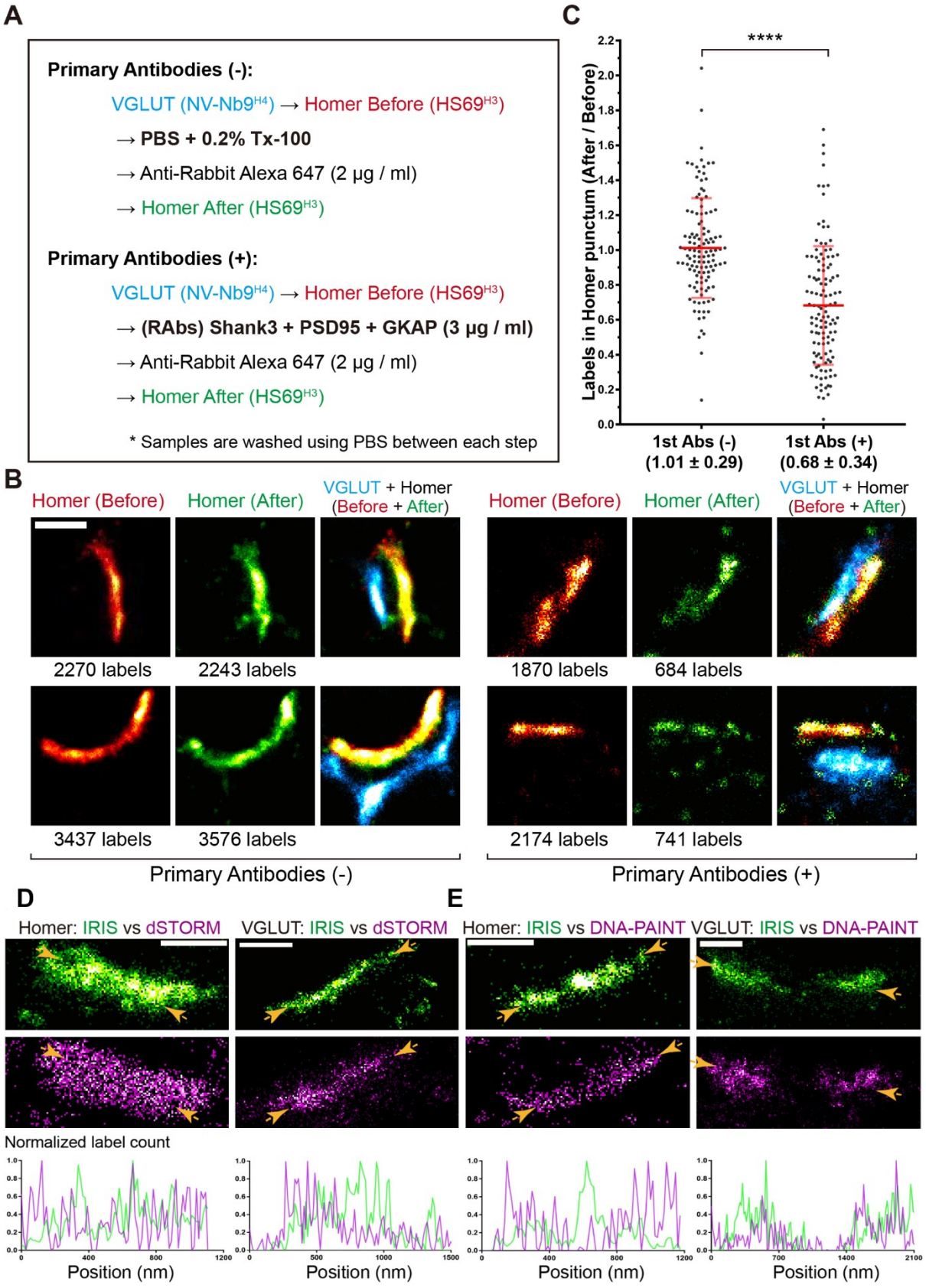

(A) Design of the experiment to examine the spatial interference of antibodies inside the post-synaptic region. The antibody incubation time is 90 min for primary antibodies and 60 min for secondary antibodies.

(B) Representative IRIS super-resolution images of VGLUT and Homer puncta in the experiment described in panel **(A)**. Imaging parameters of the Homer are the same before and after the antibody incubation. The label number of Homer probes is shown at the bottom of each image. Scale bars, 500 nm.

(C) The ratio of Homer labels after and before antibody incubation at each punctum. The data are from 120 puncta in 3 experiments, DIV21-24 for primary antibodies (-) and 120 puncta in 4 experiments, DIV21-28 for primary antibodies (+). The label ratio of Homer puncta in primary antibodies incubated samples are significantly lower than the primary antibody free samples (unpaired two-tailed t-test, **** $p < 0.0001$). Red bars show the mean ± SD.

(D) Representative super-resolution images of VGLUT or Homer puncta acquired by IRIS and dSTORM in the same neuron samples. $HS69^{H3}$ (1 nM) or NV-$Nb9^{H4}$ probes (1 nM) were first applied to neuron to perform IRIS imaging (Homer: 500 ms exposure, 20,000 frames, 2.03×10^6 localizations acquired; VGLUT: 300 ms exposure, 25,000 frames, 2.29×10^6 localizations acquired). The sample were subsequently subject to 8 times of PBS washing, 90 min of primary antibody incubation (1:500 in PBS-0.2% Tx-100), 3 times of PBS washing and 60 min of secondary antibody incubation (anti-Rabbit Alexa 647, 1:1000 in PBS-0.2% Tx-100). dSTORM imaging was perform as previously described[57] in the oxygen scavenging buffer containing 50 mM MEA at 671 nm for excitation and 488 nm for activation (Homer: 200 ms exposure, 40,000 frames, 2.10×10^6 localizations acquired; VGLUT: 100 ms exposure, 40,000 frames, 2.26×10^6 localizations acquired). The excitation intensity was adjusted so that the exposure time was half the average on-state lifetime of fluorophores. The activation 488 nm laser was used for 50 ms every 1,000 frames to keep the fluorophore density at 0.025-0.1/μm^2. Line profile between the arrow heads is shown beneath each panel. Scale bars, 500 nm.

(E) Representative super-resolution images of VGLUT or Homer puncta acquired by IRIS and DNA-PAINT in the same neuron samples. $HS69^{H3}$ (1 nM) or NV-$Nb9^{H4}$ probes (1 nM) were first applied to neuron to perform IRIS imaging (Homer: 500 ms exposure, 40,000 frames, 1.04×10^6 localizations acquired; VGLUT: 300 ms exposure, 35,000 frames, 3.83×10^6 localizations acquired). The sample were then washed 8 times by PBS and incubated with primary antibodies (1:500 in PBS-0.2% Tx-100) for 90 min. The successive steps were conducted according to manufacturer instruction of MASSIVE-AB 2-PLEX DNA-PAINT kit (Imager strand: 0.25 nM for the both targets, Homer: 200 ms exposure, 4,000 frames, 1.12×10^6 localizations acquired; VGLUT: 300 ms exposure, 30,000 frames, 3.78×10^6 localizations acquired). Line profile between the arrow heads is shown beneath each panel. Scale bars, 500 nm.

Fig. 16 Comparison of synapse imaging by IRIS, STORM and DNA-PAINT

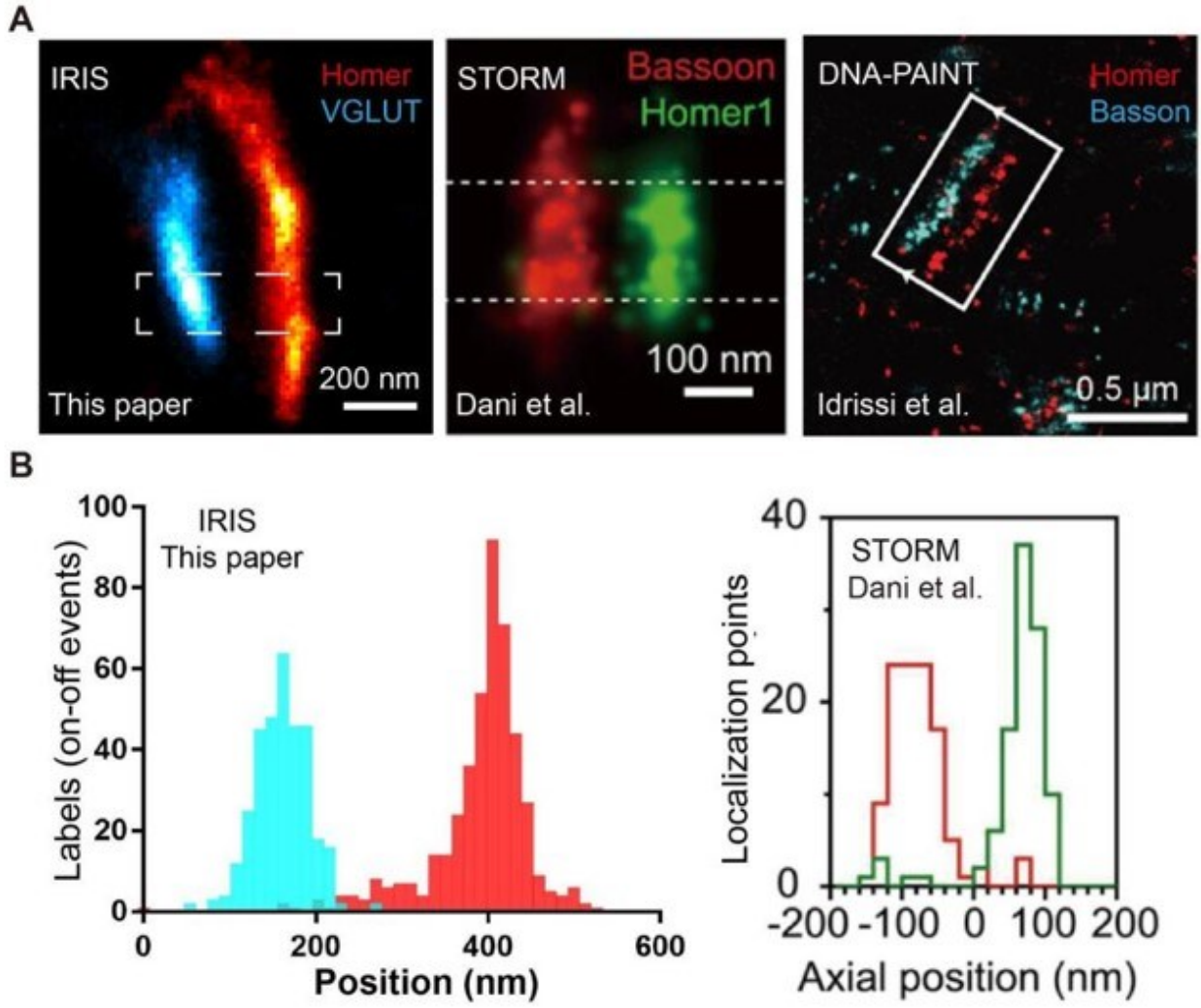

(A) IRIS image is a synapse of rat primary neurons in **Fig. 15B** (upper left) of this paper. STORM image is a synapse in brain cortex section, which is reproduced from Figure 3D in the previous study[55]. DNA-PAINT image is a synapse of rat primary neurons, reproduced from Fig. 3I in the previous study[58].

(B) Distribution of localization points (within a ~160 nm thick region between the dashed lines) along the trans-synaptic axis of IRIS image and STORM image in **(A)**. Distribution of localization points in STORM image is reproduced from the Figure 3D of the reference[55].

Table 1 Summary of mutation sites and dissociation rates of Fv-EGFP and Nb-EGFP mutants.

Clone Number	Antigen	Mutant code	Mutation site 1	Mutation site 2	Mutation site 3	Mutation site 4	Mutant koff (1/s)	Mutant half-life (s)
P20.1	TARGET	WT					0.0330	21.0
P20.1	**TARGET**	**H1L0**	**HY59G**				**0.332**	**2.09**
P20.1	TARGET	H2L0	HT28A	HY59G			0.360	1.92
P20.1	TARGET	H3L0	HY27A	HY59G			nr	nr
P20.1	TARGET	H4L1	HY27G	HT28A	LY32A		2.65	0.261
12CA5	HA	WT					0.00621	112
12CA5	HA	H1L0	HF27G				0.0254	27.3
12CA5	HA	H1L2	HF27G	LY49A			0.0358	19.4
12CA5	HA	H2L2	HF27A	LY49A			0.0292	23.7
12CA5	HA	H3L0	HT28A				0.0136	51.0
12CA5	HA	H4L0	HT28A	HY32V			0.0763	9.09
12CA5	HA	H5L0	HY32A				0.0225	3.08
12CA5	HA	H5L2	HY32A	LY49A			0.335	2.07
12CA5	**HA**	**H6L2**	**HT28A**	**HY32A**	**LY49A**		**0.601**	**1.15**
12CA5	HA	H7L0	HY59A				0.00742	93.4
12CA5	HA	H8L0	HY32G				nr	nr
12CA5	HA	H0L2	LY49A				0.0150	46.1
2H8	FLAG	WT					0.00803	91.1
2H8	FLAG	H1L0	HY59A				0.0163	42.6
2H8	**FLAG**	**H1L3**	**HS28A**	**LY96A**			**0.407**	**1.70**
2H8	FLAG	H2L3	HY59A	LY96A			0.218	3.19
2H8	FLAG	H3L0	HY102A				0.0146	47.4
2H8	FLAG	H4L3	HS28A	HY59A	LY96A		nr	nr
2H8	FLAG	H0L1	LY32A				nr	nr
2H8	FLAG	H0L2	LY49A				0.0183	37.9
2H8	FLAG	H0L3	LY96A				0.151	4.58
V302A	V5	WT					0.0322	21.5
V302A	V5	H0L1	LY32A				0.322	2.15
V302A	V5	H1L0	HY27A	HY59A			0.0624	11.1
V302A	V5	H2L0	HY27G				0.0628	11.0
V302A	**V5**	**H2L1**	**HY27G**	**LY32A**			**0.567**	**1.22**
V302A	V5	H2L2	HY27G	LY49A			nr	nr
V302A	V5	H2L3	HY27G	LY96A			nr	nr
V302A	V5	H3L0	HY27G	HY59A			nr	nr
V302A	V5	H4L0	HY59G				nr	nr
S66B	S	WT					0.139	4.97
S66B	**S**	**H1L0**	**HS28A**				**0.276**	**2.51**
S66B	S	H2L0	HF27G				0.153	4.53

NbALFA	ALFA	WT								<0.0000348	>1.99 × 10^4
NbALFA	ALFA	H1	E53A		R60A		V99A			0.00202	343
NbALFA	**ALFA**	**H2**	**V27G**	**T28A**	**Y37A**	**&**	**E53A**	**R60A**	**V99A**	**0.331**	**2.10**
HS69	Homer	WT								0.000897	773
HS69	Homer	H1	S27G		T28A					0.00777	89.2
HS69	Homer	H2	S27G		T28A		Y59A			0.0189	36.6
HS69	**Homer**	**H3**	**S27G**		**T28A**		**F37A**		**Y59A**	**0.0971**	**7.13**
HS69	Homer	H4	S27G		T28A		F37G		Y59A	nr	nr
HS69	Homer	H5	S27G		T28A		F37A		Y59G	nr	nr
NV-Nb9	VGLUT	WT								0.00164	423
NV-Nb9	VGLUT	H1	Y32A							0.00543	128
NV-Nb9	VGLUT	H2	R27G		T28A		Y102A			0.00415	167
NV-Nb9	VGLUT	H3	R27G		T28A		F37A		Y102A	0.0162	42.9
NV-Nb9	**VGLUT**	**H4**	**R27G**		**T28A**	**Y32A**	**F37A**		**Y102A**	**0.0923**	**7.14**

nr: no recognition. Bold: Mutants which were used in IRIS imaging.

References

1 Rust, M. J., Bates, M. & Zhuang, X. Sub-diffraction-limit imaging by stochastic optical reconstruction microscopy (STORM). *Nat Methods* **3**, 793-795 (2006). https://doi.org:10.1038/nmeth929

2 Abbe, E. Beiträge zur Theorie des Mikroskops und der mikroskopischen Wahrnehmung. *Archiv für mikroskopische Anatomie* **9**, 413-418 (1873). https://doi.org:10.1007/bf02956173

3 Hell, S. W. Far-field optical nanoscopy. *Science* **316**, 1153-1158 (2007). https://doi.org:10.1126/science.1137395

4 Heintzmann, R. & Huser, T. Super-Resolution Structured Illumination Microscopy. *Chem Rev* **117**, 13890-13908 (2017). https://doi.org:10.1021/acs.chemrev.7b00218

5 Lelek, M. *et al.* Single-molecule localization microscopy. *Nat Rev Methods Primers* **1** (2021). https://doi.org:10.1038/s43586-021-00038-x

6 Kiuchi, T., Higuchi, M., Takamura, A., Maruoka, M. & Watanabe, N. Multitarget super-resolution microscopy with high-density labeling by exchangeable probes. *Nat Methods* **12**, 743-746 (2015). https://doi.org:10.1038/nmeth.3466

7 Shroff, H., Galbraith, C. G., Galbraith, J. A. & Betzig, E. Live-cell photoactivated localization microscopy of nanoscale adhesion dynamics. *Nat Methods* **5**, 417-423 (2008). https://doi.org:10.1038/nmeth.1202

8 Miyoshi, T. *et al.* Semi-automated single-molecule microscopy screening of fast-dissociating specific antibodies directly from hybridoma cultures. *Cell Rep* **34**, 108708 (2021). https://doi.org:10.1016/j.celrep.2021.108708

9 Vallet-Courbin, A. *et al.* A Recombinant Human Anti-Platelet scFv Antibody Produced in Pichia pastoris for Atheroma Targeting. *PLoS One* **12**, e0170305 (2017). https://doi.org:10.1371/journal.pone.0170305

10 Ill, C. R. *et al.* Design and construction of a hybrid immunoglobulin domain with properties of both heavy and light chain variable regions. *Protein Engineering, Design and Selection* **10**, 949-957 (1997). https://doi.org:10.1093/protein/10.8.949

11 Sela-Culang, I., Kunik, V. & Ofran, Y. The structural basis of antibody-antigen recognition. *Front Immunol* **4**, 302 (2013). https://doi.org:10.3389/fimmu.2013.00302

12 Lehmann, A. *et al.* Stability engineering of anti-EGFR scFv antibodies by rational design of a lambda-to-kappa swap of the VL framework using a structure-guided approach. *MAbs* **7**, 1058-1071 (2015). https://doi.org:10.1080/19420862.2015.1088618

13 Kang, T. H. & Seong, B. L. Solubility, Stability, and Avidity of Recombinant Antibody Fragments Expressed in Microorganisms. *Front Microbiol* **11**, 1927 (2020). https://doi.org:10.3389/fmicb.2020.01927

14 Arimori, T. *et al.* Fv-clasp: An Artificially Designed Small Antibody Fragment with Improved Production Compatibility, Stability, and Crystallizability. *Structure* **25**, 1611-1622 e1614 (2017). https://doi.org:10.1016/j.str.2017.08.011

15 Watson, J. F., Pinggera, A., Ho, H. & Greger, I. H. AMPA receptor anchoring at CA1 synapses is determined by N-terminal domain and TARP γ8 interactions. *Nat Commun* **12**, 5083 (2021). https://doi.org:10.1038/s41467-021-25281-4

16 Watanabe, N. & Mitchison, T. J. Single-molecule speckle analysis of actin filament turnover in lamellipodia. *Science* **295**, 1083-1086 (2002). https://doi.org:10.1126/science.1067470

17 Yamashiro, S. *et al.* New single-molecule speckle microscopy reveals modification of the retrograde actin flow by focal adhesions at nanometer scales. *Mol Biol Cell* **25**, 1010-1024 (2014). https://doi.org:10.1091/mbc.E13-03-0162

18 Zhou, H., Fisher, R. J. & Papas, T. S. Optimization of primer sequences for mouse scFv repertoire display library construction. *Nucleic Acids Res* **22**, 888-889 (1994). https://doi.org:10.1093/nar/22.5.888

19 Ikeda, K. *et al.* Generation and characterization of a human-mouse chimeric high-affinity antibody that detects the DYKDDDDK FLAG peptide. *Biochem Biophys Res Commun* **486**, 1077-1082 (2017). https://doi.org:10.1016/j.bbrc.2017.03.165

20 Götzke, H. *et al.* The ALFA-tag is a highly versatile tool for nanobody-based bioscience applications. *Nat Commun* **10**, 4403 (2019). https://doi.org:10.1038/s41467-019-12301-7

21 Dong, J. X. *et al.* A toolbox of nanobodies developed and validated for use as intrabodies and nanoscale immunolabels in mammalian brain neurons. *Elife* **8** (2019). https://doi.org:10.7554/eLife.48750

22 Schenck, S. *et al.* Generation and Characterization of Anti-VGLUT Nanobodies Acting as Inhibitors of Transport. *Biochemistry* **56**, 3962-3971 (2017). https://doi.org:10.1021/acs.biochem.7b00436

23 Suzuki, J. *et al.* Imaging intraorganellar Ca2+ at subcellular resolution using CEPIA. *Nat Commun* **5**, 4153 (2014). https://doi.org:10.1038/ncomms5153

24 Al-Lazikani, B., Lesk, A. M. & Chothia, C. Standard conformations for the canonical structures of immunoglobulins. *J Mol Biol* **273**, 927-948 (1997). https://doi.org:10.1006/jmbi.1997.1354

25 Dunbar, J. & Deane, C. M. ANARCI: antigen receptor numbering and receptor classification. *Bioinformatics* **32**, 298-300 (2016). https://doi.org:10.1093/bioinformatics/btv552

26 Sircar, A., Sanni, K. A., Shi, J. & Gray, J. J. Analysis and modeling of the variable region of camelid single-domain antibodies. *J Immunol* **186**, 6357-6367 (2011). https://doi.org:10.4049/jimmunol.1100116

27 Zhou, R., Han, B., Xia, C. & Zhuang, X. Membrane-associated periodic skeleton is a signaling platform for RTK transactivation in neurons. *Science* **365**, 929-934 (2019). https://doi.org:10.1126/science.aaw5937

28 Xu, K., Zhong, G. & Zhuang, X. Actin, spectrin, and associated proteins form a periodic cytoskeletal structure in axons. *Science* **339**, 452-456 (2013). https://doi.org:10.1126/science.1232251

29 Shi, X., Lim, J. & Ha, T. Acidification of the oxygen scavenging system in single-molecule fluorescence studies: in situ sensing with a ratiometric dual-emission probe. *Anal Chem* **82**, 6132-6138 (2010). https://doi.org:10.1021/ac1008749

30 Blumhardt, P. *et al.* Photo-Induced Depletion of Binding Sites in DNA-PAINT Microscopy. *Molecules* **23** (2018). https://doi.org:10.3390/molecules23123165

31 Olivier, N., Keller, D., Gönczy, P. & Manley, S. Resolution doubling in 3D-STORM imaging through improved buffers. *PLoS One* **8**, e69004 (2013). https://doi.org:10.1371/journal.pone.0069004

32 Descloux, A., Grußmayer, K. S. & Radenovic, A. Parameter-free image resolution estimation based on decorrelation analysis. *Nat Methods* **16**, 918-924 (2019). https://doi.org:10.1038/s41592-019-0515-7

33 Kuglin, C. D. & Hines, D. C. The phase correlation image alignment method. *Proc. Int. Conf. on Cybernetics and Society, 1975*, 163-165 (1975).

34 Tabata, S. *et al.* A rapid screening method for cell lines producing singly-tagged recombinant proteins using the "TARGET tag" system. *J Proteomics* **73**, 1777-1785 (2010). https://doi.org:10.1016/j.jprot.2010.05.012

35 Zimmermann, K., Hoischen, S., Hafner, M. & Nischt, R. Genomic Sequences and Structural Organization of the Human Nidogen Gene (NID). *Genomics* **27**, 245-250 (1995). https://doi.org:https://doi.org/10.1006/geno.1995.1038

36 Schymeinsky, J. *et al.* Gene structure and functional analysis of the mouse nidogen-2 gene: nidogen-2 is not essential for basement membrane formation in mice. *Mol Cell Biol* **22**, 6820-6830 (2002). https://doi.org:10.1128/mcb.22.19.6820-6830.2002

37 Suzuki, J. *et al.* Imaging intraorganellar Ca2+ at subcellular resolution using CEPIA. *Nature Communications* **5**, 4153 (2014). https://doi.org:10.1038/ncomms5153

https://www.nature.com/articles/ncomms5153#supplementary-information

38 Borden, P. & Kabat, E. A. Nucleotide sequence of the cDNAs encoding the variable region heavy and light chains of a myeloma protein specific for the terminal nonreducing end of alpha(1----6)dextran. *Proc Natl Acad Sci U S A* **84**, 2440-2443 (1987). https://doi.org:10.1073/pnas.84.8.2440

39 Krause, K.-H. & Michalak, M. Calreticulin. *Cell* **88**, 439-443 (1997). https://doi.org:10.1016/S0092-8674(00)81884-X

40 Fujii, Y. *et al.* PA tag: a versatile protein tagging system using a super high affinity antibody against a dodecapeptide derived from human podoplanin. *Protein Expr Purif* **95**, 240-247 (2014). https://doi.org:10.1016/j.pep.2014.01.009

41 Koide, S. & Sidhu, S. S. The importance of being tyrosine: lessons in molecular recognition from minimalist synthetic binding proteins. *ACS Chem Biol* **4**, 325-334 (2009). https://doi.org:10.1021/cb800314v

42 Tsumoto, K. *et al.* Role of Tyr Residues in the Contact Region of Anti-lysozyme Monoclonal Antibody HyHEL10 for Antigen Binding. *Journal of Biological Chemistry* **270**, 18551-18557 (1995). https://doi.org:10.1074/jbc.270.31.18551

43 Sela-Culang, I., Kunik, V. & Ofran, Y. The structural basis of antibody-antigen recognition. *Frontiers in immunology* **4**, 302-302 (2013). https://doi.org:10.3389/fimmu.2013.00302

44 Haidar, J. N. *et al.* A universal combinatorial design of antibody framework to graft distinct CDR sequences: a bioinformatics approach. *Proteins* **80**, 896-912 (2012). https://doi.org:10.1002/prot.23246

45 Betapudi, V. Myosin II motor proteins with different functions determine the fate of lamellipodia extension during cell spreading. *PLoS One* **5**, e8560 (2010). https://doi.org:10.1371/journal.pone.0008560

46 Tojkander, S. *et al.* A molecular pathway for myosin II recruitment to stress fibers. *Curr Biol* **21**, 539-550 (2011). https://doi.org:10.1016/j.cub.2011.03.007

47 Burnette, D. T. *et al.* A contractile and counterbalancing adhesion system controls the 3D shape of crawling cells. *J Cell Biol* **205**, 83-96 (2014). https://doi.org:10.1083/jcb.201311104

48 Thul, P. J. *et al.* A subcellular map of the human proteome. *Science* **356** (2017). https://doi.org:10.1126/science.aal3321

49 Andrews, N. P. *et al.* A toolbox of IgG subclass-switched recombinant monoclonal antibodies for enhanced multiplex immunolabeling of brain. *Elife* **8** (2019). https://doi.org:10.7554/eLife.43322

50 Ye, X. & Cai, Q. Snapin-mediated BACE1 retrograde transport is essential for its degradation in lysosomes and regulation of APP processing in neurons. *Cell Rep* **6**, 24-31 (2014). https://doi.org:10.1016/j.celrep.2013.12.008

51 Ilardi, J. M., Mochida, S. & Sheng, Z. H. Snapin: a SNARE-associated protein implicated in synaptic transmission. *Nat Neurosci* **2**, 119-124 (1999). https://doi.org:10.1038/5673

52 Sidenstein, S. C. *et al.* Multicolour Multilevel STED nanoscopy of Actin/Spectrin Organization at Synapses. *Sci Rep* **6**, 26725 (2016). https://doi.org:10.1038/srep26725

53 Wilhelm, B. G. *et al.* Composition of isolated synaptic boutons reveals the amounts of vesicle trafficking proteins. *Science* **344**, 1023-1028 (2014). https://doi.org:10.1126/science.1252884

54 Sugiyama, Y., Kawabata, I., Sobue, K. & Okabe, S. Determination of absolute protein numbers in single synapses by a GFP-based calibration technique. *Nat Methods* **2**, 677-684 (2005). https://doi.org:10.1038/nmeth783

55 Dani, A., Huang, B., Bergan, J., Dulac, C. & Zhuang, X. Superresolution imaging of chemical synapses in the brain. *Neuron* **68**, 843-856 (2010). https://doi.org:10.1016/j.neuron.2010.11.021

56 Tao-Cheng, J. H., Azzam, R., Crocker, V., Winters, C. A. & Reese, T. Depolarization of Hippocampal Neurons Induces Formation of Nonsynaptic NMDA Receptor Islands Resembling Nascent Postsynaptic Densities. *eNeuro* **2** (2015). https://doi.org:10.1523/ENEURO.0066-15.2015

57 van de Linde, S. *et al.* Direct stochastic optical reconstruction microscopy with standard fluorescent probes. *Nat Protoc* **6**, 991-1009 (2011). https://doi.org:10.1038/nprot.2011.336

58 Sograte-Idrissi, S. *et al.* Circumvention of common labelling artefacts using secondary nanobodies. *Nanoscale* **12**, 10226-10239 (2020). https://doi.org:10.1039/d0nr00227e

59 Huang, B., Bates, M. & Zhuang, X. Super-resolution fluorescence microscopy. *Annu Rev Biochem* **78**, 993-1016 (2009). https://doi.org:10.1146/annurev.biochem.77.061906.092014

60 Jungmann, R. *et al.* Multiplexed 3D cellular super-resolution imaging with DNA-PAINT and Exchange-PAINT. *Nat Methods* **11**, 313-318 (2014). https://doi.org:10.1038/nmeth.2835

61 Agasti, S. S. *et al.* DNA-barcoded labeling probes for highly multiplexed Exchange-PAINT imaging. *Chem Sci* **8**, 3080-3091 (2017). https://doi.org:10.1039/c6sc05420j

62 Klevanski, M. *et al.* Automated highly multiplexed super-resolution imaging of protein nano-architecture in cells and tissues. *Nat Commun* **11**, 1552 (2020). https://doi.org:10.1038/s41467-020-15362-1

63 Guo, S. M. *et al.* Multiplexed and high-throughput neuronal fluorescence imaging with diffusible probes. *Nat Commun* **10**, 4377 (2019). https://doi.org:10.1038/s41467-019-12372-6

64 Gunasekara, H., Munaweera, R. & Hu, Y. S. Chaotropic Perturbation of Noncovalent Interactions of the Hemagglutinin Tag Monoclonal Antibody Fragment Enables Superresolution Molecular Census. *ACS Nano* (2021). https://doi.org:10.1021/acsnano.1c04237

65 Dunbar, J. *et al.* SAbDab: the structural antibody database. *Nucleic Acids Res* **42**, D1140-1146 (2014). https://doi.org:10.1093/nar/gkt1043

66 Lima, W. C. *et al.* The ABCD database: a repository for chemically defined antibodies. *Nucleic Acids Res* **48**, D261-D264 (2020). https://doi.org:10.1093/nar/gkz714

67 Tanaka, T., Thomas, J., Van Montfort, R., Miller, A. & Rabbitts, T. Pan RAS-binding compounds selected from a chemical library by inhibiting interaction between RAS and a reduced affinity intracellular antibody. *Sci Rep* **11**, 1712 (2021). https://doi.org:10.1038/s41598-021-81262-z

68 Yamashita, T. *et al.* Affinity Improvement of a Cancer-Targeted Antibody through Alanine-Induced Adjustment of Antigen-Antibody Interface. *Structure* **27**, 519-527.e515 (2019). https://doi.org:10.1016/j.str.2018.11.002

69 Clark, L. A. *et al.* Affinity enhancement of an in vivo matured therapeutic antibody using structure-based computational design. *Protein Sci* **15**, 949-960 (2006). https://doi.org:10.1110/ps.052030506

Acknowledgements

I sincerely thank my supervisor Prof. Naoki Watanabe for supervising this study and providing me so much insightful advice. I thank Dr. Akitoshi Miyamoto and Dr. Takushi Miyoshi (NIH) for giving me good experimental training and providing invaluable suggestions. I thank Dr. Sawako Yamashiro for providing essential materials and helpful advices for this study. I am also grateful to Prof. Tai Kiuchi, Prof. Junichi Takagi (Osaka University), Prof. Takao Arimori (Osaka University) and Dr. Shin Watanabe for their continuous technical support for this research.

I would like to thank Miss Kayoko Fukumitsu and Miss Emiko Nishimoto for their great assistance. I also thank all the members in Watanabe Lab: They gave me precious suggestions and encouragement anytime I faced problems.

I appreciate MEXT for providing the stipends when I first came to Japan. I was a recipient of Special Research Fellowship from Kobayashi Foundation in doctoral course. These scholarships greatly support my research career and daily life.

Finally, I would like to thank my family members: my parents, my grandparent and my fiancée for their great love and warm encouragement during these years.

This thesis is based on the material contained in the following article.

Qianli Zhang, Akitoshi Miyamoto, Shin Watanabe, Takao Arimori, Masanori Sakai, Madoka Tomisaki, Tai Kiuchi, Junichi Takagi and Naoki Watanabe
Engineered fast-dissociating antibody fragments for multiplexed super-resolution microscopy
Cell Reports Methods 2, 100301, October 24, 2022
DOI: https://doi.org/10.1016/j.crmeth.2022.100301